



Rapid and ultrasensitive electromechanical detection of ions, biomolecules and SARS-CoV-2 RNA in unamplified samples

Liqian Wang^{1,2,3,8}, Xuejun Wang^{1,2,3,8}, Yungen Wu^{1,2,3,8}, Mingquan Guo^{4,8}, Chenjian Gu⁵, Changhao Dai^{1,2,3}, Derong Kong^{1,2,3}, Yao Wang⁵, Cong Zhang^{1,2,3}, Di Qu⁵, Chunhai Fan⁶, Youhua Xie⁵, Zhaoqin Zhu⁴✉, Yunqi Liu^{3,7} and Dacheng Wei^{1,2,3}✉

The detection of samples at ultralow concentrations (one to ten copies in 100 μ l) in biofluids is hampered by the orders-of-magnitude higher amounts of ‘background’ biomolecules. Here we report a molecular system, immobilized on a liquid-gated graphene field-effect transistor and consisting of an aptamer probe bound to a flexible single-stranded DNA cantilever linked to a self-assembled stiff tetrahedral double-stranded DNA structure, for the rapid and ultrasensitive electromechanical detection (down to one to two copies in 100 μ l) of unamplified nucleic acids in biofluids, and also of ions, small molecules and proteins, as we show for Hg²⁺, adenosine 5'-triphosphate and thrombin. We implemented an electromechanical biosensor for the detection of SARS-CoV-2 into an integrated and portable prototype device, and show that it detected SARS-CoV-2 RNA in less than four minutes in all nasopharyngeal samples from 33 patients with COVID-19 (with cycle threshold values of 24.9–41.3) and in none of the 54 COVID-19-negative controls, without the need for RNA extraction or nucleic acid amplification.

Owing to the ultralow abundance of many disease-relevant biomarkers, ultraprecise analysis of trace analytes in bulk biofluids (that is, approximately one to ten copies in 100 μ l) is of great significance for biological research, precision medicine and early-stage diagnosis^{1–4}. Such a precise analysis can approach the physical limit of biosensors, which is inevitably affected by the large amounts of non-specific proteins, nucleic acids or other background biomolecules^{2,4–6}. Some techniques can monitor single molecules or few molecules by using nanometre-sized transducers, leveraging tiny testing volumes and ultrasmall recognition cross-sections, yet they inherently lack molecular-level sensitivity in a bulk matrix³. Despite efforts made during the past few decades, ultraprecise biodetection remains a critical problem in the chemical and biological sciences, and faces increasing requirements, especially in the context of the coronavirus disease 2019 (COVID-19) pandemic and other large-scale epidemics^{7–12}. Owing to challenges in the detection of ultralow concentrations of target molecules in testing solutions^{10,12}, direct severe acute respiratory syndrome coronavirus 2 (SARS-CoV-2) nucleic acid testing has not been employed for clinical COVID-19 diagnosis. Without sufficient sensitivity, the established methodologies—that is, those based on quantitative reverse-transcription polymerase chain reaction (qRT-PCR)—require nucleic acid extraction and amplification procedures, which need skilled technicians, specific laboratories and equipment, and long processing times (>2h); hence, on-site and point-of-care SARS-CoV-2 nucleic acid testing remains a hurdle^{7–12}. Despite

target amplifications larger than 10⁶-fold, the limit of detection (LoD) of the qRT-PCR assay is typically ~0.2–1 copies per μ l (~0.3 \times 10⁻¹⁸ to 1.7 \times 10⁻¹⁸ M)^{7–10,13}. Assays for nucleic acid testing that are simple, rapid and ultraprecise would contribute to slowing down the fast spreading of SARS-CoV-2 (ref. ¹⁴).

Microelectromechanical systems (MEMS) are typically highly integrated, small, inexpensive and highly efficient, with feasibility for commercialization^{15–18}. MEMS integrate micrometre-scale mechanical components with microelectronics, to convert mechanical, chemical, biological or other sensing responses to electrical signals^{15,16,18}. Via integration with field-effect transistors (FETs), MEMS could make ultrasensitive biosensors, in particular because FETs combine efficient transducers with signal amplifiers in which a small parameter alteration induces a pronounced change of channel current^{1,19–24}. Because smaller dimensions enable measurements with higher sensitivity and resolution^{16–18}, by miniaturizing feature sizes down to submicrometre scales, nanoelectromechanical systems (NEMS) reduce cost, volume, weight and power consumption while improving sensing performance^{15–17}. However, the performance of these systems remains far below that of many living systems, in which biorecognition and responses typically occur via exquisitely precise molecular-level mechanisms²⁵.

For biosensors based on MEMS, NEMS and FETs, without designing the sensing interface and manipulating the systems at the molecular level, the sensitivity rarely reaches 10⁻¹⁷ M (~600 copies in 100 μ l) in bulk buffer or diluted biofluids^{5,6,19–21,26–31}. Such sensitivity

¹State Key Laboratory of Molecular Engineering of Polymers, Fudan University, Shanghai, China. ²Department of Macromolecular Science, Fudan University, Shanghai, China. ³Laboratory of Molecular Materials and Devices, Fudan University, Shanghai, China. ⁴Department of Laboratory Medicine, Shanghai Public Health Clinical Center, Fudan University, Shanghai, China. ⁵Key Laboratory of Medical Molecular Virology (MOE/NHC/CAMS), Department of Medical Microbiology and Parasitology, School of Basic Medical Sciences, Shanghai Medical College, Fudan University, Shanghai, China. ⁶Frontiers Science Center for Transformative Molecules, School of Chemistry and Chemical Engineering, Institute of Molecular Medicine, Renji Hospital, School of Medicine, Shanghai Jiao Tong University, Shanghai, China. ⁷Institute of Chemistry, Chinese Academy of Sciences, Beijing, China. ⁸These authors contributed equally: Liqian Wang, Xuejun Wang, Yungen Wu, Mingquan Guo. ✉e-mail: zhaqinzh@163.com; weidc@fudan.edu.cn

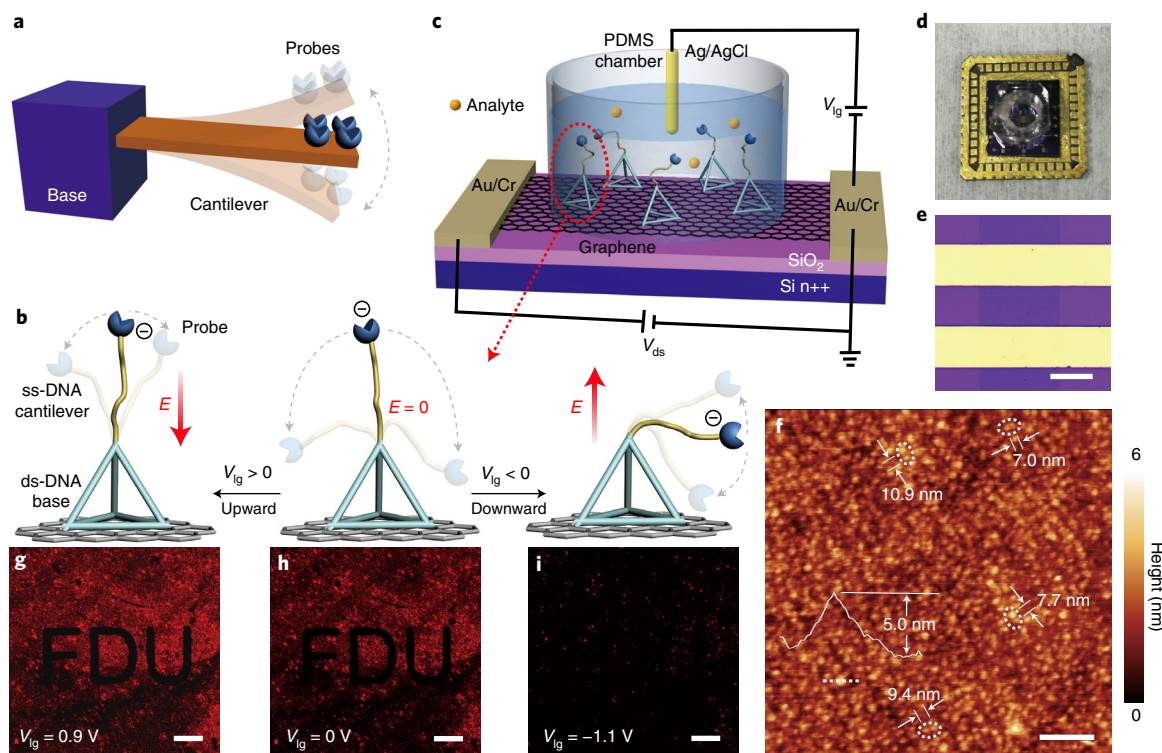


Fig. 1 | MoEMS and MoEMS g-FET. **a**, Schematic of biodetection by MEMS or NEMS. **b**, Schematic of MoEMS and its electrostatic actuation. A probe is conjugated at the tip of the ss-DNA cantilever, for specific biorecognition. E indicates an electric field. **c**, The device configuration of a MoEMS g-FET. **d,e**, Photograph (**d**) and optical microscope image (**e**) of the device. **f**, AFM image (in $1\times$ TM buffer) of graphene immobilized with MoEMSs. The colour bar indicates the height of the scanned surface. **g–i**, Fluorescence intensity images of graphene immobilized with Cy3-17bp-15T MoEMSs where V_{lg} is 0.9 V (**g**), 0 V (**h**) and -1.1 V (**i**). Cy3 is conjugated at the tip of ss-DNA cantilever as the fluorescence dye. Scale bars, 100 nm (**f**) and 30 μm (**e–i**).

is hardly maintained in complex and high-ionic-strength biofluids. Some molecular-scale systems relying on chemical-binding-induced geometry changes have recently been developed for chemical sensing^{21,32,33}. However, their detection sensitivity is normally $\sim 10^{-14}$ – 10^{-6} M. In this Article, we show that a molecular electromechanical system (MoEMS) consisting of an aptamer probe bound to a flexible single-stranded DNA (ss-DNA) cantilever linked to a self-assembled stiff tetrahedral double-stranded DNA (ds-DNA) structure enables the ultrasensitive and specific detection of proteins, small molecules, ions and nucleic acids in biofluids. In particular, MoEMS enables the direct detection of SARS-CoV-2 RNA in nasopharyngeal swab samples with concentrations down to ~ 0.02 copies per μl RNA in viral transport medium (VTM).

Results

Structure and actuation of MoEMS. MoEMS has two parts: a stiff base and a flexible cantilever. The base has a tetrahedral structure with six ds-DNA edges linked by single-stranded hinges^{34,35}. A flexible ss-DNA, which serves as a cantilever, extends from one strand of the tetrahedral base via a spacer consisting of thymine nucleotides, and ends in a pendant probe (Fig. 1a,b). Here, the probe is an aptamer, which is a short, single-stranded oligonucleotide with a specific three-dimensional structure^{36–38}. Depending on the structure, the aptamer can fold into or around the complex surface of target molecule via shape-dependent, hydrophobic, base-stacking or intercalation interactions³⁹. Aptamers are widely used to recognize a variety of targets with high affinity and specificity, including small molecules, proteins, ions, nucleic acids and cells, for diverse diagnostic, therapeutic, imaging and gene-regulation applications³⁹.

MoEMS structures are self-assembled in $1\times$ TM (Tris-HCl, MgCl₂) buffer by mixing several complementary ss-DNAs

(Supplementary Table 1). Agarose gel electrophoresis (Supplementary Fig. 1) and fluorescence resonance energy transfer (FRET; Supplementary Fig. 1) analysis demonstrate the assemblage of MoEMSs. The MoEMS structures are then immobilized on the channel of a liquid-gated graphene FET (g-FET) (Supplementary Note 1, Fig. 1c–e and Supplementary Figs. 2–5). The appearance of an X-ray photoelectron spectroscopy P 2p peak (Supplementary Fig. 6) indicates the immobilization of the MoEMS structures. Atomic force microscopy (AFM) images measured in $1\times$ TM buffer (Fig. 1f and Supplementary Fig. 7) shows that the MoEMS structures (17bp-5T: 17 base pairs for the tetrahedral edges, 5 thymine nucleotides for the cantilever spacer) are maintained, and that they are uniformly anchored on the entire graphene surface with a density of $\sim 3\times 10^3$ to 4×10^3 μm^{-2} . No aggregation was observed. The MoEMS structures appear as individual pyramids with a height around 5 nm and a lateral distance larger than 7 nm, in good agreement with the designed structure. As a comparison, ss-DNA aptamers on graphene tend to collapse and aggregate (Supplementary Fig. 8), with morphologies different from those of the MoEMS structures.

The ss-DNA cantilever functions similarly to those in MEMS and NEMS. One side is connected to the rigid base, while the other side is free to ‘surf’ in solution (with a larger degree of movement than when bound on a flat surface). The ss-DNA cantilever has higher flexibility than cantilevers in conventional MEMS and NEMS, allowing for actuation at the molecular scale. Owing to the phosphates in the DNA backbone, the cantilever is negatively charged⁴⁰. When applying a positive or negative gate voltage by the liquid electrolyte (V_{lg}), a local electrical field lifts up or pushes down the cantilever, leading to confined cantilever movements in the upper or lower regions of the MoEMS, respectively (Fig. 1b).

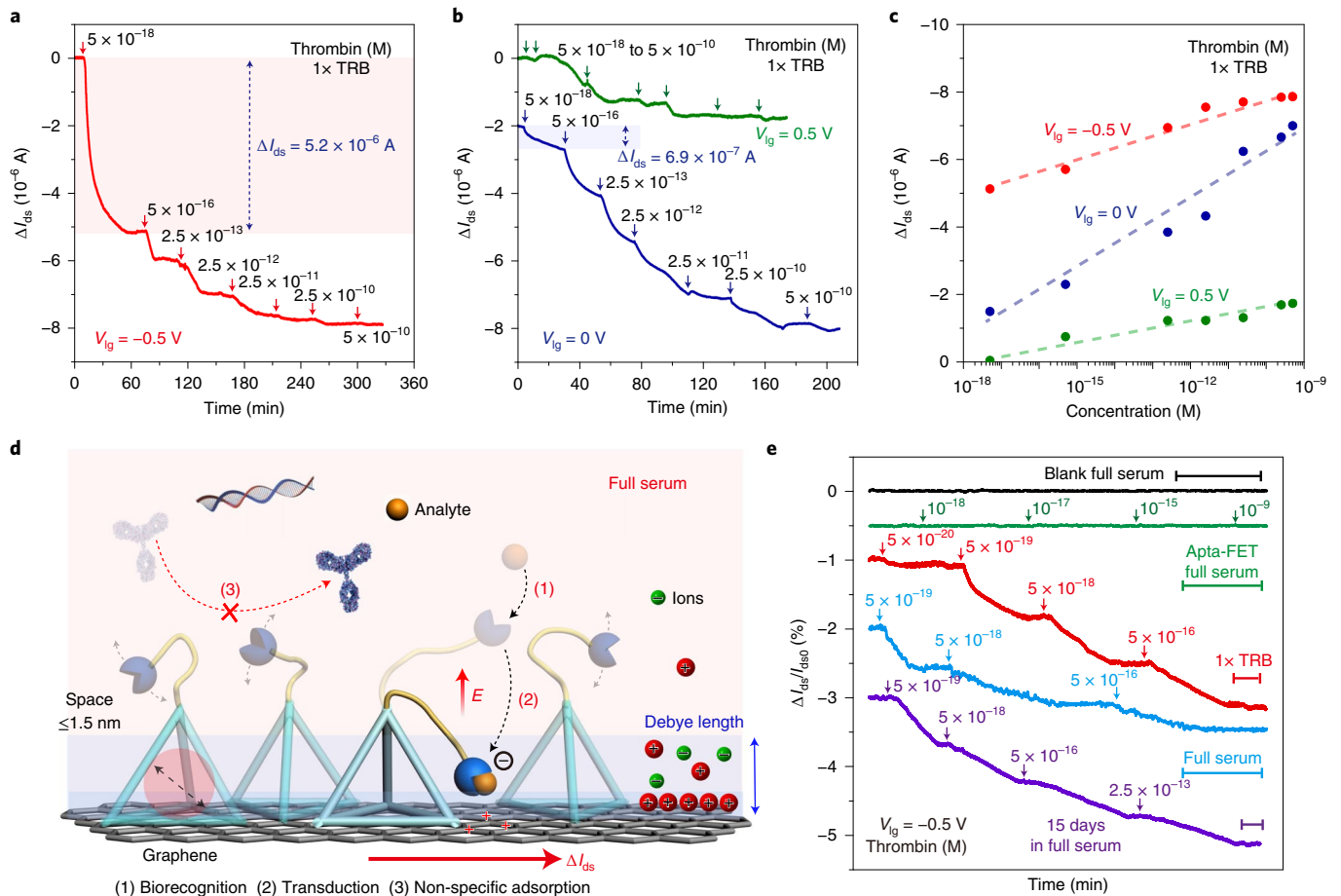


Fig. 2 | Ultrasensitive biodetection and long-term stability. **a–c**, Real-time ΔI_{ds} responses (**a,b**) and ΔI_{ds} (**c**) of a g-FET modified with TBA-functionalized MoEMS on the addition of thrombin (from 5×10^{-18} M to 5×10^{-10} M) in $1 \times$ TRB buffer, at $V_{lg} = -0.5$ V (**a,c**), 0 V (**b,c**) and 0.5 V (**b,c**). **d**, Sensing mechanism of MoEMS. Owing to their high coverage of the surface, the rigid bases avoid non-specific adsorption. The probes on the flexible cantilevers recognize the targets specifically. On electrostatic actuation, the recognition events are detected in the g-FET channel, leading to efficient biorecognition and signal transduction. **e**, $\Delta I_{ds}/I_{ds0}$ versus t curves of g-FETs with TBA-functionalized MoEMS in full serum (black) and upon the sequential addition of thrombin in $1 \times$ TRB buffer (red) or full serum (blue). The green curve is measured in full serum by a g-FET with a TBA-functionalized 5T aptamer (Apta-FET). The purple curve corresponds to a g-FET with TBA-functionalized MoEMS after 15 days of incubation in full serum. Scale bars, 20 min. All the tested samples were technical replicates.

To examine such actuation, we conjugated a fluorescent dye Cyanine3 (Cy3) (rather than a probe) at the tip of the cantilever. Cy3 fluorescence quenching by graphene occurred at negative V_{lg} (Fig. 1g–i and Supplementary Figs. 9–11), indicating the electrostatic actuation of the cantilever as well as the upright configuration of MoEMS, which allows the ss-DNA cantilever to face upwards and to have sufficient space for actuation. At $V_{lg} = -0.9$ V or -1.1 V, the relative intensity was comparable to or lower than that of Cy3-conjugated DNA tetrahedron with 7 bp edges (Supplementary Fig. 12); thus, the actual distance between the Cy3 and graphene decreased to ~ 2 nm or smaller (Supplementary Note 2).

Ultraprecise biodetection by MoEMS g-FETs. The unique structure as well as the molecular-level actuation of MoEMS enables ultraprecise biodetection in bulk biofluids (Fig. 2). Biochemical sensing involves specific biorecognition and signal transduction^{1–5,19–31,34}. A high density of 17bp-5T MoEMS structures was accommodated on the graphene surface with a highly ordered upright orientation and controllable distance³⁴, which ensured a large free space for cantilever movements and prevented them from entanglements, local aggregation and non-covalent adsorption on the graphene surface (Supplementary Fig. 8)⁴¹. In fact, the probes

on the cantilevers should move freely and stay active. The high density of MoEMS structures on the large-area channel surface of the g-FETs allowed for efficient recognition of ultralow concentrations of analytes. Graphene is an atomically thick material with extremely high mobility, in which all carriers flow solely on the surface. Thus, g-FETs promise highly efficient signal transduction to minute electrochemical perturbations associated with the analytes in solution⁴². However, efficient signal transduction faces a Debye-length limitation in ionic solution, because potential perturbations in response to recognition events beyond the Debye length are screened by the electrical double layer (Supplementary Note 3). The Debye length is a measure of a charge carrier's net electrostatic effect in a solution and of how far its electrostatic effect persists. Effective recognition events need to occur within the Debye length, and the value is normally less than 1 nm in high-ionic-strength buffer and biofluids^{21,23,24}.

MoEMS overcomes such a limitation. The base height of 17bp-5T is around 5.3 nm, approximately the cantilever length (6.8 nm). When $V_{lg} > 0$ V or $V_{lg} = 0$ V, the cantilever moves in the upper region or randomly in a wide region, respectively. Thus, there is a small chance that the recognized analytes move approaching the graphene surface within the Debye length. When applying a negative

V_{lg} , the local electrical field actuates the cantilevers downwards, and its movements become confined to the lower region of MoLEMSs. More of the recognized analytes therefore come close to the graphene's surface. Owing to the electrostatic or doping effect, the recognized events within the Debye length lead to variations of the electrical potential of the graphene channel, in a way that is similar to applying an external potential to the gate electrode in conventional FETs. Then, conductivity changes, and a current response associated with the analytes occurs in the channel in real time⁴². Therefore, the actuation of MoLEMS at negative V_{lg} enhances the current response. Considering this as well as the intrinsic amplification and ultrahigh sensitivity of g-FETs^{19–31,42}, we expect the signal transduction to be efficient (Supplementary Note 4).

We functionalized the cantilever with a 15-mer thrombin-binding aptamer (TBA) with a G-quadruplex structure, as a probe for thrombin recognition⁴³. At $V_{lg} = -0.5$ V, we measured the drain–source current (I_{ds}) versus time (t) on successive additions of thrombin with concentrations from 5×10^{-18} to 5×10^{-10} M in $1 \times$ thrombin-binding (TRB) buffer. I_{ds} decreased with increasing concentration before reaching saturation, in agreement with the evolution of the $I_{ds} - V_{lg}$ curves at different concentrations of thrombin (Supplementary Fig. 13). ΔI_{ds} responses are defined as I_{ds} (at each concentration) $- I_{ds0}$, where I_{ds0} is the average value of I_{ds} when no sample is presented. The ΔI_{ds} response at 5×10^{-18} M thrombin is approximately seven- to eightfold larger than that at $V_{lg} = 0$ V (Fig. 2a–c), which is consistent with the divergence of the $I_{ds} - V_{lg}$ curve (Supplementary Fig. 14). At $V_{lg} = 0.5$ V, only negligible ΔI_{ds} responses occur at 5×10^{-18} M (Fig. 2b,c). Under actuation at $V_{lg} = -0.5$ V, 5×10^{-20} M thrombin in $1 \times$ TRB buffer generated obvious ΔI_{ds} responses (Fig. 2e), around eight orders of magnitude lower than those of thrombin FET sensors previously reported²⁷. Therefore, MoLEMS enables both efficient biorecognition and signal transduction, giving rise to ultrahigh sensitivity.

In practice, most biosensors cannot achieve ultrahigh sensitivities in biofluids, especially in full serum, because non-specific nucleic acids, proteins and other background biomolecules crowd the sensing interfaces, blocking the active sites, generating background noise and depressing the long-term stability of the sensors^{2–5}. To reduce non-specific adsorption, anti-fouling layers such as bovine serum albumin (BSA), peptides and zwitterionic polymers can be applied. However, these layers can block the active sites, and hence they impose a trade-off in detection sensitivity³. In fact, using a BSA anti-fouling layer on the graphene surface blocked the actuation of the ss-DNA cantilevers and decreased the sensitivity of the g-FETs (Supplementary Figs. 15–17). MoLEMS does not suffer from this problem, sidestepping the trade-off between bare sensitivity and anti-fouling ability (Supplementary Note 5). Owing to their high density, the rigid bases with a 5.3 nm height serve as an anti-fouling layer, which resists non-target biomolecules larger than 1.5 nm in diameter, avoiding non-specific adsorption and keeping them away from the channel (Fig. 2d). We measured the hysteresis of $I_{ds} - V_{lg}$ curves, performed in situ AFM and determined $\Delta I_{ds}/I_{ds0}$ responses on BSA addition as well as electrical-field-driven Cy3 fluorescence quenching in full serum (Supplementary Figs. 18 and 19 and Extended Data Fig. 1), and the results demonstrate the excellent anti-fouling feature of MoLEMS. At the same time, MoLEMS maintains high sensitivity. The probes on the flexible cantilevers recognize the targets specifically, and such recognition events are transferred down to the graphene surface on actuation, leading to efficient biorecognition and signal transduction. To clarify this mechanism, we used Cy3-conjugated 17bp-15T on the graphene surface. Cy3 fluorescence quenching at negative V_{lg} still occurs in full serum (Supplementary Figs. 15 and 16), indicating that the ss-DNA cantilevers remain operative in challenging biological environments. As a comparison, we modified the graphene with a BSA anti-fouling layer. No obvious Cy3 fluorescence quenching occurred, indicating the blocking effect of conventional anti-fouling materials.

In full serum, MoLEMS g-FETs have $\Delta I_{ds}/I_{ds0}$ responses (Fig. 2e) on the addition of thrombin ranging from 5×10^{-19} to 5×10^{-16} M when actuating at $V_{lg} = -0.5$ V. g-FETs modified with a TBA-5T aptamer have no $\Delta I_{ds}/I_{ds0}$ response even when thrombin concentration increases by ten orders of magnitude to 10^{-9} M. We continuously exposed the devices to full serum for 15 days at 4°C. MoLEMS g-FETs still produced obvious $\Delta I_{ds}/I_{ds0}$ responses (Fig. 2e) at thrombin concentrations ranging from 5×10^{-19} M to 2.5×10^{-13} M in full serum. The $\Delta I_{ds}/I_{ds0}$ responses of MoLEMS g-FETs with DH25.42 aptamer probes (Extended Data Fig. 2) were maintained at ~56% on the addition of 5×10^{-15} M adenosine 5'-triphosphate (ATP) in full serum after 15 days of incubation, indicating the long-term stability of MoLEMS g-FETs in biofluids.

Universality, specificity and structural design of MoLEMS g-FETs. MoLEMS g-FETs can be used to specifically detect different categories of analytes. Cantilevers of 17bp-5T were functionalized with DH25.42 aptamer⁴³, oligodeoxynucleotide aptamer³⁷ or a complementary oligonucleotide (Supplementary Table 1) to specifically detect ATP, Hg^{2+} and targeted ss-DNA (ss-DNA-T), respectively. When actuating MoLEMS by V_{lg} , the detectable concentration of ATP and Hg^{2+} (Fig. 3a,b and Extended Data Fig. 3) reached 5×10^{-20} M in $1 \times$ ATP $MgCl_2$ (AM) or $1 \times$ Tris $MgCl_2$ (TM) buffer (Supplementary Note 3), orders of magnitude lower than previous ATP and Hg^{2+} FET sensors^{28,29}. Owing to the high density of the active probes, the signal of some devices did not reach a saturation even when the concentration increased to 5×10^{-10} M, showing the wide detection range of the sensors. In full serum, obvious $\Delta I_{ds}/I_{ds0}$ responses were observed on the addition of ATP or ss-DNA-T as low as 5×10^{-20} M (Supplementary Fig. 23). Non-target proteins (BSA, casein), ions (Fe^{3+} , Cd^{2+} , Zn^{2+} , Ca^{2+} , Cu^{2+}), nucleoside triphosphates (cytidine 5'-triphosphate (CTP), guanosine 5'-triphosphate (GTP)), three ss-DNA strands with random sequences (ss-DNA-R1 to R3) and three ss-DNA strands (ss-DNA-mis-3', ss-DNA-mis-m, ss-DNA-mis-5') with one-base mismatches at different locations (Supplementary Table 1) could be measured at a concentration ten times higher than the targets (Fig. 3c and Extended Data Fig. 4) and the mixture samples with the targets (Extended Data Fig. 5). Negligible responses were observed on the addition of non-target analytes. These results suggest that MoLEMS g-FETs are a universal technology for biodetection with high specificity.

We also investigated the structural design of MoLEMS. The ability to design the sequences from the bottom-up to self-assemble into specific DNA structures allows for the construction of functional systems with predicted structures and conformations^{34,35}. We prepared four TBA-functionalized DNA structures (Fig. 3d and Supplementary Fig. 1), including 5T (6.8 nm ss-DNA), 17bp-5T, 17bp-15T (5.3 nm base with 10.2 nm cantilever) and 37bp-5T (11.1 nm base with 6.8 nm cantilever). The direct modification of TBA-5T aptamers on g-FETs led to small Dirac point shifts and to negligible ΔI_{ds} responses ($V_{lg} = 0$ V and -0.5 V) on the addition of thrombin (Supplementary Fig. 20). An obvious shift of the Dirac point (Fig. 3e) only occurred when using 17bp-5T, indicating that the ΔI_{ds} response is originated from the potential change associated with the recognition of thrombin and that an appropriate size ratio for the base and the cantilever is critical for ultraprecise biodetection (Supplementary Note 6). Moreover, device geometry and the structural design of MoLEMS g-FETs are also important for the sensing performance. Molecular diffusion is normally slow under ambient conditions. Using polydimethylsiloxane (PDMS) wells with low height-to-width ratios and adding analytes via pre-mixed samples can improve both the speed and sensitivity of detection (Supplementary Figs. 21 and 22 and Supplementary Note 7).

Unamplified SARS-CoV-2 nucleic acid testing. We applied MoLEMS g-FETs to the detection of SARS-CoV-2 RNA. Nucleic acid

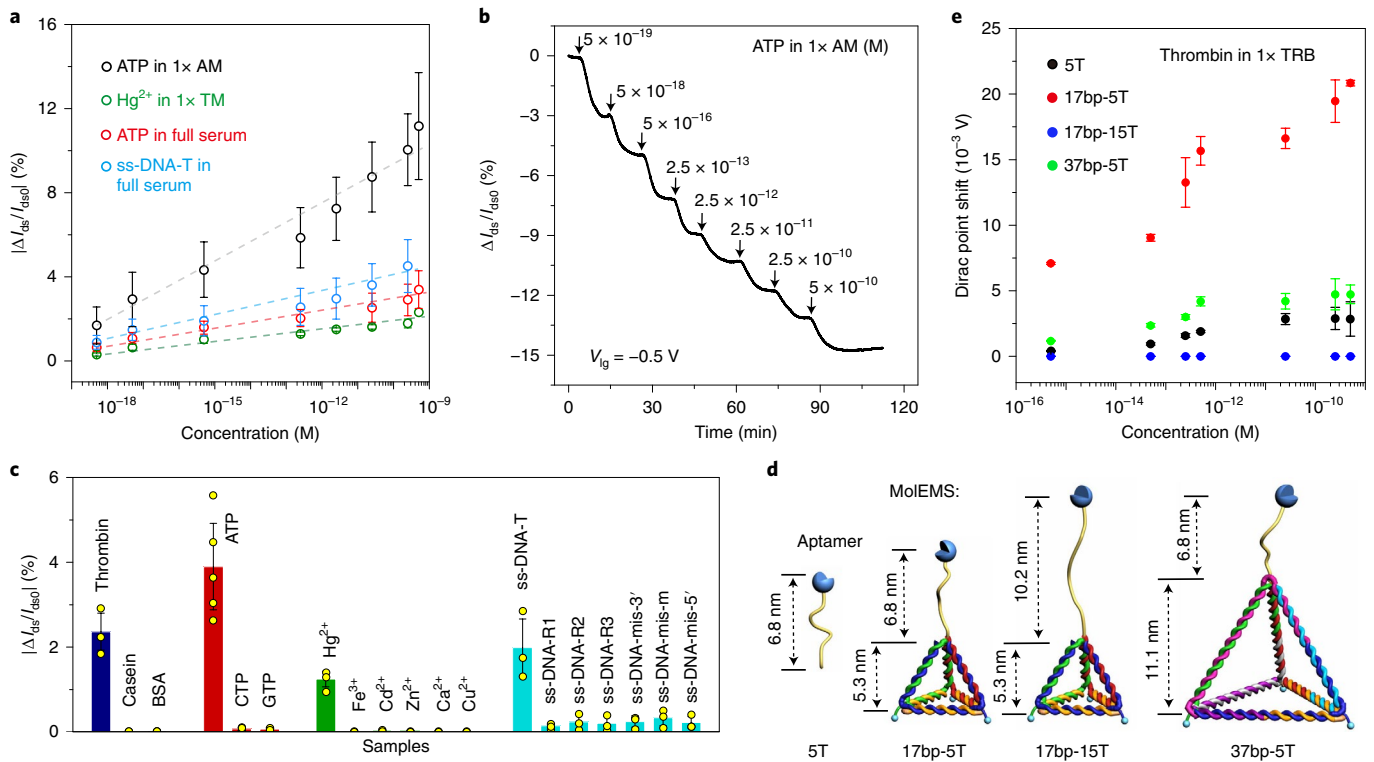


Fig. 3 | Universality, specificity and structural design. **a, b**, $|\Delta I_{ds}/I_{dso}|$ (**a**) and real-time $\Delta I_{ds}/I_{dso}$ (**b**) responses at different concentrations of ATP (1× AM), Hg^{2+} (1× TM), ATP (full serum) and ss-DNA-T (full serum) under electrostatic actuation of MoEMS with the corresponding probes. **c**, $|\Delta I_{ds}/I_{dso}|$ responses of MoEMS g-FETs on the addition of target analytes (5×10^{-16} M) and non-target (5×10^{-15} M) analytes. **d**, Schematic illustration of four DNA structures. **e**, Dirac-point shift as a function of thrombin concentration when using different DNA structures ($V_{ds} = 50$ mV). The error bars in **a**, **c** and **e** are defined by the standard deviation of the results from at least three parallel experiments. All the tested samples were technical replicates.

tests for COVID-19 typically require time-consuming nucleic acid extraction and amplification procedures (Fig. 4a)^{7–10}. We show that MoEMS g-FETs can be used for direct SARS-CoV-2 nucleic acid testing. We functionalized cantilever tips with probes targeting either SARS-CoV-2 RNA or reverse-transcribed complementary DNA for the *ORF1ab* gene (nt13377–13404, Fig. 4b and Supplementary Table 1). We tested the devices with five samples spiked in full artificial saliva: cDNA reverse-transcribed from SARS-CoV-2 viral RNA from a patient with confirmed COVID-19 with severe pneumonia (sample 1, Supplementary Fig. 23), SARS-CoV-2 in vitro transcribed (IVT) RNA (sample 2), SARS-CoV IVT RNA (sample 3), Middle East respiratory syndrome coronavirus (MERS-CoV) IVT RNA (sample 4) and human cDNA (sample 5).

Real-time $\Delta I_{ds}/I_{dso}$ responses on the addition of sample 1 or sample 2 with concentrations ranging from 1.67×10^{-19} M (0.1 copies per μ l) to 8.33×10^{-17} M (500 copies per μ l) in full artificial saliva were recorded under electrostatic actuation (Fig. 4c and Supplementary Fig. 24). In Supplementary Table 2 (see also Supplementary Note 8), we provide the square root of the sum of the squares of dilution (σ_{RSS}) and Poisson errors (σ_p), which show the uncertainties of the analyte copies in sample preparation. $\Delta I_{ds}/I_{dso}$ responses were detected with a reaction time as short as 4 min. ΔI_{ds} was 2.4×10^{-7} A at 0.1 copies per μ l, consistent with the calculated ΔI_{ds} for a few copies of SARS-CoV-2 cDNA (Supplementary Note 4). The LoD reached ~ 0.01 – 0.02 copies per μ l for sample 1 and sample 2 (Supplementary Figs. 25, Extended Data Fig. 6 and Supplementary Note 9), equivalent to approximately one to two copies in 80 μ l of artificial saliva. Near the LoD, some devices showed responses (Supplementary Fig. 26). We measured 20 devices, and 15 out of 20 showed responses for 0.025 copies per μ l of SARS-CoV-2 cDNA in 80 μ l of artificial saliva. The average response time was ~ 6.5 min (Supplementary Fig. 27).

MoEMS g-FETs (inset of Fig. 4c) distinguished SARS-CoV-2 nucleic acids from human cDNA (sample 5) and from related coronavirus IVT RNA (sample 3 and sample 4).

Direct SARS-CoV-2 nucleic acid testing of clinical samples. Measuring clinical samples brings in higher biological complexity, as well as uncertainties arising from differences between patients and from sample collection and preparation procedures. Moreover, SARS-CoV-2 RNA is about 30,000 nucleotides, and hence it involves complex folding structures. We tested 33 nasopharyngeal swab samples ($\sim P1$ – $P33$) from patients with qRT-PCR-positive COVID-19 with cycle threshold (Ct) values ranging from 24.9 to 41.3 (Supplementary Table 3), 23 samples ($\sim F1$ – $F23$) from qRT-PCR-negative patients with fever, 6 samples from patients with influenza A or B ($\sim A1$ – $A4$, B1, B2) and 25 samples ($\sim H1$ – $H25$) from healthy volunteers. All clinical samples followed a heating process to release nucleic acids and were then tested directly without nucleic acid extraction or amplification (Fig. 4a). Although the VTM contained background biomolecules and possibly contamination, SARS-CoV-2 RNA from $\sim P1$ – $P33$ could be detected directly by the MoEMS g-FETs with $\Delta I_{ds}/I_{dso}$ in the range of 0.8–6.85%. The rest of the samples led to negligible signals (mostly $\Delta I_{ds}/I_{dso} < 0.08\%$) (Fig. 4d,e, Extended Data Fig. 6, Supplementary Figs. 28–30 and Supplementary Table 3). The overall agreement with the qRT-PCR results was perfect. The time to COVID-19 diagnosis ($\sim P1$ – $P26$) was ~ 0.1 –4 min with an average of 60 s (inset of Fig. 4d), when $\Delta I_{ds}/I_{dso}$ reached three times the initial $\Delta I_{ds}/I_{dso}$ value. MoEMS g-FETs responded to 6% diluted P1 (Fig. 4d) as well as to P18, with a Ct value of 41.3 (Extended Data Fig. 7), indicating high sensitivity when testing clinical samples.

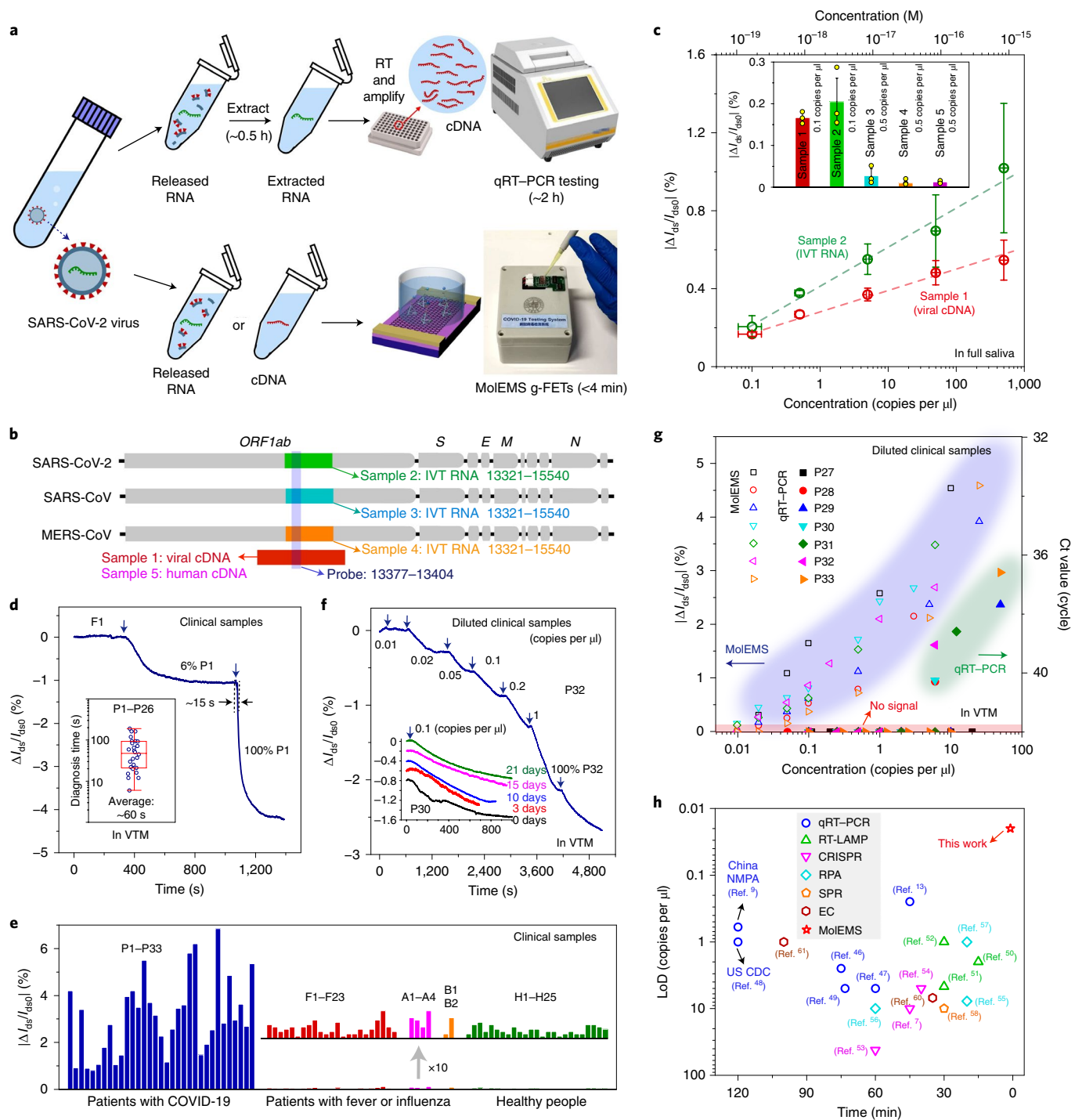


Fig. 4 | SARS-CoV-2 nucleic acid testing. **a**, Workflows for SARS-CoV-2 nucleic acid testing by qRT-PCR and MolEMS g-FETs. **b**, Genome map showing the selected sequences (and their relative positions) used for the probes and for samples 1-5. S, spike protein gene; E, envelope protein gene; M, membrane protein gene; N, nucleocapsid protein gene. **c**, $|\Delta I_{ds}/I_{ds0}|$ responses upon the addition of sample 1 and sample 2 (from 0.1 to 500 copies per μl) (technical replicates) in full artificial saliva. The inset shows the selectivity in the presence of target analytes (0.1 copies per μl) and non-target analytes (0.5 copies per μl) (technical replicates) in full artificial saliva. The error bars are defined by the standard deviation of the results from at least three parallel experiments. **d**, $\Delta I_{ds}/I_{ds0}$ versus t curve on the addition of F1, 6% P1 and 100% P1 (biological replicates). The inset is the box plot (indicating the interquartile range and the minimum and maximum values) of the diagnosis time for the clinical samples P1-P26 (biological replicates). **e**, $|\Delta I_{ds}/I_{ds0}|$ responses corresponding to each clinical sample. 'x10' indicates ten times the $|\Delta I_{ds}/I_{ds0}|$ (for F1-F23, A1-A4, B1, B2 and H1-H25; biological replicates). **f**, $\Delta I_{ds}/I_{ds0}$ versus t curve of diluted P32 with concentrations from 0.01 copies per μl in VTM to 100% P32 (biological replicates). The inset is $\Delta I_{ds}/I_{ds0}$ versus t curves of the devices on the addition of 0.1 copies per μl of P30 (biological replicates) after 0, 3, 10, 15 and 21 days incubation in VTM. **g**, $|\Delta I_{ds}/I_{ds0}|$ responses and Ct values of diluted -P27-P33 (biological replicates) in VTM. **h**, Comparison of MolEMS (this work) with SARS-CoV-2 nucleic acid detection by qRT-PCR, US CDC or China-NMPA-approved qRT-PCR, RT-LAMP, CRISPR, RPA, SPR and EC.

To test for device sensitivity, we quantified the clinical samples ~P27–P33 according to Ct values and the qRT–PCR standard curve (Supplementary Fig. 31), and diluted them serially using VTM. We extracted the viral nucleic acids from the diluted samples, and then measured them by qRT–PCR (detection kit DA0931 from DaAn Gene). Negligible qRT–PCR signals were captured at low concentrations. As a comparison, $\Delta I_{ds}/I_{ds0}$ responses on the addition of the diluted samples occurred even when the concentration decreased to ~0.02 copies per μl in VTM (Fig. 4f,g). We rinsed the device with VTM to remove non-specifically adsorbed species. No obvious change of I_{ds} occurred during the rinsing step (Supplementary Fig. 32), indicating anti-fouling against unspecific binding in the clinical samples. Moreover, we stored the devices in VTM at 4 °C for 21 days. $\Delta I_{ds}/I_{ds0}$ responses at 0.1 copies per μl of diluted P30 in VTM were maintained (inset of Fig. 4f), indicating the long-term stability of the MoEMS g-FETs.

Fast assays for COVID-19 diagnosis have been developed recently. In particular, antigen testing by FET devices has enabled detection in minutes^{44,45}. Nucleic acid testing is regarded as the gold standard for COVID-19 diagnosis, owing to its high accuracy^{3,14}. Compared with commercial detection kits (Supplementary Table 4) and COVID-19 assays (Fig. 4h and Supplementary Table 5), including qRT–PCR^{13,46–49}, US Centers for Disease Control (CDC)/China National Medical Products Administration (NMPA)-approved qRT–PCR assays^{8,9}, reverse transcription loop-mediated isothermal amplification (RT-LAMP)^{50–52}, clustered regularly interspaced short palindromic repeats (CRISPR)^{7,53,54}, recombinase polymerase amplification (RPA)^{55–57}, surface plasmon resonance (SPR)⁵⁸, electrochemical devices (EC)^{59–61} and antigen/antibody testing^{44,45,62,63}, MoEMS g-FETs may be advantageous in that it offers rapid detection of SARS-CoV-2 nucleic acids, easy operation, high sensitivity and specificity, and portability.

Discussion

Compared with MEMS and NEMS, MoEMS reduces cost, volume and weight, and allows for molecular-level manipulation. Under electrostatic actuation, MoEMS allows for the specific detection of proteins, small molecules, ions and nucleic acids, down to 5×10^{-20} M in high-ionic-strength buffer or biofluids, even after 15 days of continuous exposure to full serum. MoEMS is a most sensitive biosensor with anti-fouling ability, detection selectivity, stability and universality^{2,5,6,21}. We have shown that MoEMS g-FETs allow for the direct testing of unamplified SARS-CoV-2 nucleic acids with concentrations down to ~0.02 copies per μl in nasopharyngeal swab samples. The devices also allow for rapid and label-free detection, and for easy operation. In particular, in clinical samples, MoEMS detected COVID-19 in ~0.1–4 min (faster than qRT–PCR) without the requirement for RNA extraction. Further development of portable systems (Supplementary Figs. 33 and 34) could enable on-site and point-of-care testing in airports, clinics and local emergency departments and even at home. Besides COVID-19, the development of MoEMS could allow for the ultraprecise diagnosis of other diseases in a few minutes, without the need for target purification, amplification or culture, which normally requires hours or days. Furthermore, the design principles of MoEMS could be useful beyond biosensing, for the design of other electromechanical devices and functional systems with higher precision.

Methods

Graphene growth. Monolayer graphene was produced by chemical vapour deposition, as reported previously⁶⁴. Cu foil (25 μm thick) was placed in the centre of a tube furnace (GSL 1200X), and was heated to 1,000 °C under a 4 standard cubic centimetres per minute (sccm) flow of H_2 (99.999%) for 30 min. After that, the Cu foil was annealed at 1,000 °C in 4 sccm H_2 for another 30 min. Then, 16 sccm CH_4 (99.999%) was introduced as the carbon source in the atmosphere of 4 sccm H_2 . The growth lasted for 15 min. Finally, the tube furnace was

immediately cooled to room temperature under H_2 gas. The graphene film on the Cu foil was transferred to a SiO_2/Si substrate by the electrochemical bubbling method⁶⁵.

Fabrication of g-FETs. The g-FET device was fabricated via a thermally assisted bilayer lift-off process⁶⁶. Two layers of resist (sacrificial layer LOR 3 A and photoresist S1813) were sequentially spin-coated on the SiO_2/Si wafer. After photolithography (Microwriter ML3, Durham Magneto Optics), 5/45 nm Cr/Au was deposited by using a thermal evaporator (Angstrom Engineering). The sample was heat treated on a hot plate at 170 °C for 1 min to allow photoresist reflow. Due to the higher reflow temperature of LOR (MicroChem LOR series reflow temperature >250 °C, DOW MicroPosit S1800 series reflow temperature <200 °C), the bottom photoresist undercut remains un-deformed while the top layer deformed. The introduced gap allowed the Remover PG stripper solution to access the photoresist, and improved the efficiency of the lift-off process considerably. The sample was treated by oxygen plasma to remove the photoresist residues. Graphene synthesized by chemical vapour deposition was then transferred onto the wafer using poly(methyl methacrylate) (PMMA) carrier layer to connect the drain and the source electrodes⁶⁷. PMMA was subsequently removed by acetone. Finally, the graphene was patterned via standard photolithography and O_2 plasma etching techniques to define the sensing region. Typically, the width and length of the graphene channel were 60 μm and 30 μm , respectively.

Synthesis of MoEMS. MoEMS was obtained by self-assembling four oligonucleotides. The sequences of the oligonucleotides were designed as listed in Supplementary Table 1, and then were prepared and purified by Sangon Biotechnology. Once received, we centrifuged the tubes at 10,200 rpm at 4 °C for 5 min, then dissolved the DNA powder in ultrapure water (18.2 M Ω , Milli-Q system). The concentrations of ss-DNA stock solutions were calculated on the basis of their absorbance at 260 nm using ultraviolet-visible spectroscopy (Lambda750, Perkin-Elmer) through the Beer–Lambert law⁶⁸: $A = \epsilon bc$, where A is the absorbance, ϵ is the molar absorptivity, b is the optical path length and c is the molar concentration. Equimolar quantities at a final concentration (1 μM) of four strands for the assemblage of the MoEMSs were mixed in 1 \times TM buffer at 95 °C for 10 min, and were cooled to 4 °C immediately using a thermal cycler (SimpliAmp, Thermo Fisher Scientific)⁶⁹. Then, the MoEMSs were obtained, which contained a stiff base and a flexible cantilever. The base had a tetrahedral structure with six ds-DNA edges linked by single-stranded hinges, and each vertex at the bottom carried an amino group. The cantilever was an ss-DNA with thymine nucleotide spacer (5 T or 15 T) and a probe at the tip. Here, the probe was TBA aptamer, DH25.42 aptamer and oligodeoxynucleotide aptamer for detecting thrombin, ATP and Hg^{2+} , respectively, or complementary oligonucleotide for detecting ss-DNA-T, cDNA and RNA. Finally, the MoEMSs were stored in 1 \times TM buffer at 4 °C for later use.

Fabrication of MoEMS g-FETs. The immobilization of MoEMS involves non-covalently functionalizing 1-pyrenebutanoic acid succinimidyl ester (PASE, Sigma-Aldrich) on monolayer chemical-vapour-deposition graphene (Supplementary Fig. 3) via π – π stacking, and covalently linking PASE to the amino groups at the bottom of the base of MoEMS. The g-FET device was immersed in a dimethylformamide (Sigma-Aldrich) solution of 5 mM PASE for 1.5 h at room temperature⁷⁰. The PASE molecules served as linkers, which were terminated to the graphene via π – π interactions between graphene and the pyrene groups of PASE. A PDMS well was stamped above the graphene channel to hold the solution. After rinsing thoroughly with ethanol and ultrapure water, 50 μl 1 \times TM buffer with 100 nM MoEMS was added in the PDMS well for 12 h at room temperature. Following this incubation, the solution in PDMS well was changed to 100 mM ethanolamine (Sigma-Aldrich) in 1 \times TM buffer solution for 1 h, which deactivated and blocked the excess reactive groups remaining on the graphene surface (Supplementary Fig. 4). Then, the solution in the PDMS well was changed to 1 \times TM buffer, and the device was rinsed at least three times. Finally, 80 μl buffer or VTM was added to the PDMS well, and it was sealed by a piece of glass or wafer. The device was stored at 4 °C in the dark.

Characterization. The morphologies of g-FET devices modified with MoEMSs and ss-DNA aptamers were analysed in fluids (1 \times TM buffer) by AFM (Fastscan, Bruke) operated in ScanAsyst mode using an ultrasharp tip (Fluid+, Bruke) of ~2–3 nm radius. In the AFM images, we determined the number of MoEMSs in a certain area on the graphene surface, and calculated the density via dividing the number by the area. The average density was obtained by measuring different locations. The g-FET devices after serum incubation were rinsed by ultrapure water and dried by nitrogen, then were analysed in air by AFM operated in ScanAsyst mode using a ~20–25 nm radius tip (Scanasyst air).

The graphene samples were measured by Raman spectrometer (LabRam HR Evolution, Horiba Jobin Yvon, 532 nm Ar ion laser) and high-resolution transmission electron microscope (Tecnai G2 F20 S-Twin, acceleration voltage 200 kV). The g-FET devices modified with MoEMSs or ss-DNA aptamers were washed thoroughly by ultrapure water, dried by nitrogen and then scanned by scanning electron microscope (Gemini SEM500, Zeiss) at 0.8 keV. MoEMSs were analysed using 3% agarose gel electrophoresis in 1 \times TBE Mg^{2+} buffer (89 mM

Tris, 89 mM boric acid, 2 mM EDTA, 12.5 mM Mg²⁺, pH ~8.0) at 95 V for 40 min, and then the gels were stained in Sybr safe (Thermo Fisher) for 30 min followed by imaging under ultraviolet exposure (Gel-doc XR+, Bio-Rad). Before and after modifying with PASE and MoEMS, the graphene was measured by X-ray photoelectron spectroscopy (Thermo Fisher Scientific K-Alpha instrument) with an Al X-ray source ($h\nu = 1,486.6$ eV).

FRET analysis was performed as follows⁷¹: (1) the DNA nanostructures with dyes were added in 1× TM buffer with a final concentration of 200 nM; (2) 400 μl solution was pipetted into a quartz cuvette and fluorescence spectra measured by fluorescence spectrometry (PTI QuantaMaster QM-40) with 514 nm excitation wavelength and 600 nm s⁻¹ scan rate; (3) the FRET efficiency (E_{FRET}) was determined from the decrease in donor fluorescence intensity via:

$$E_{\text{FRET}} = 1 - (I_{\text{DA}}/I_{\text{D}})$$

where I_{DA} and I_{D} denote the measured maximum fluorescence intensity of the donor (Cy3) for the DNA nanostructures with or without the acceptor (Cy5), respectively. The sequences (5'-3') of DNA strands used in the FRET experiments are presented in the Supplementary Table 1.

Confocal fluorescence microscopy measurement. Graphene was transferred by PMMA onto a quartz substrate with pre-patterned gold electrodes and patterns. The graphene surface was immobilized with Cy3-conjugated 17bp-15T MoEMs, Cy3-conjugated 7bp DNA nanostructures or Cy3-conjugated 17bp DNA nanostructures. A PDMS well was stamped on the top of graphene and filled with 1× TM buffer. To measure the electrical-field-driven fluorescence quenching (Supplementary Note 2), a Ag/AgCl electrode was inserted into the solution to apply a V_{lg} which generated an electrical field and drove Cy3 on 17bp-15T MoEMs downwards. The fluorescence intensities were imaged by using a confocal fluorescence microscope (C2+, Nikon)⁷².

Cells and virus. Human kidney cells HEK293 and African green monkey kidney cell line Vero E6 (Cell bank of Chinese Academy of Sciences) were cultured at 37°C with 5% CO₂ in Dulbecco's modified Eagle medium (Gibco) containing 2 mM L-glutamine, 50 U ml⁻¹ penicillin, 100 mg ml⁻¹ streptomycin and 10% (vol./vol.) foetal bovine serum (Gibco). SARS-CoV-2 strain nCoV-SH01 (GenBank, MT121215.1), from a laboratory-confirmed COVID-19 severe pneumonia case provided from CDC Shanghai, was propagated in Vero E6 cells in a biosafety level 3 laboratory⁷³.

Preparation of samples 1–5 for SARS-CoV-2 nucleic acid testing. Sample 1 and sample 5 were extracted from African green monkey kidney cell line Vero E6 and human kidney cells HEK293, respectively, by using TRIzol reagent (Invitrogen) following the manufacturer's instructions. Viral RNA or human RNA was used for synthesizing first-strand cDNA by SuperScript III CellsDirect cDNA Synthesis Kit (Invitrogen). Viral cDNA was then quantified by qRT-PCR (qRT-PCR detection kit Tiangen). For MoEMS g-FET testing, the vials containing 10⁸ copies per μl viral cDNA were centrifuged at 3,000 rpm at 4°C for 5 min and diluted into 5 × 10⁷ copies per μl first in full artificial saliva (Solarbio) and 2% of RNase inhibitor (Thermo Fisher), then were serially diluted in full artificial saliva to concentrations of 5,000,000, 500,000, 50,000, 5,000, 500, 50, 5, 0.5, 0.1 and 0.02 copies per μl.

Sample 2, sample 3 and sample 4 were SARS-CoV-2, SARS-CoV and MERS-CoV IVT RNA reference materials (nt 13321–15540, GenBank no. MT027064.1, no. NC004718.3 and no. NC019843.3), respectively, with a titre of 10⁵ copies per μl, provided by Shanghai Institute of Measurement and Testing Technology. For MoEMS g-FET testing, the samples were centrifuged at 3,000 rpm at 4°C for 5 min and diluted into 5,000 copies per μl first in full artificial saliva (Solarbio) and 2% of RNase inhibitor (Thermo Fisher), and then were serially diluted in full artificial saliva to a concentration of 500, 50, 5, 0.5 and 0.1 copies per μl.

Clinical samples. The clinical samples used were collected from Department of Laboratory Medicine, Shanghai Public Health Clinical Center. Thirty-three nasopharyngeal swab samples were from patients with qRT-PCR-positive COVID-19. Twenty-three nasopharyngeal swab samples were from qRT-PCR-negative patients in fever clinic. Four nasopharyngeal swab samples were from patients with influenza A. Two nasopharyngeal swab samples were from patients with influenza B. Other 25 nasopharyngeal swab samples were from healthy volunteers. To release the RNA, 200 μl VTM (Yocon) used to store the swab was heated at 56°C for 30 min. Then, the medium was directly used for SARS-CoV-2 nucleic acid testing by MoEMS g-FETs without requirement of the extraction procedure. This research was approved by the Shanghai Public Health Clinical Center Ethics Committee (approval ID number 2020-Y114-01) with informed consent from participants.

qRT-PCR assay. Sample 1 was extracted by TRIzol reagent (Invitrogen) following the manufacturer's instructions. Viral RNA was used for synthesizing first-strand cDNA by using SuperScript III CellsDirect cDNA Synthesis Kit (Invitrogen). To quantify viral cDNA in sample 1, qRT-PCR was performed in a 20 μl reaction (containing 2 μl cDNA sample) using qRT-PCR detection kit (Tiangen) on an MXP3000 cycler (Stratagene) as follows: 95°C 5 min; 40 cycles of 95°C 10 s, 50°C 30 s and 72°C 30 s. PCR primers (Genewiz) targeting SARS-CoV-2 RdRp gene

(nt 1113–1326) were (forward/reverse) 5'-CTTGTGTATGCTGCTGACCC-3'/5'-GCAGATTACCATCCTGAGC-3'. The copies of cDNA in sample 1 were calculated based on the standard curve (Supplementary Fig. 29).

To quantify viral RNA in clinical samples, 200 μl swab samples were extracted following instructions as described in the protocol (magnetic bead nucleic acid extraction kit, SDK60165) from Jiangsu Shuoshi Biological Technology. qRT-PCR was performed in a 25 μl reaction system by using 2019-nCoV nucleic acid detection kit (DaAn Gene). Five microlitres of the extracted nucleic acid elution sample was taken as the amplification template for amplification on Applied Biosystems 7500 (BJ001271, ABI), according to the protocol (2019-nCoV nucleic acid detection kit, DA0931). The copies of RNA in the clinical samples were calculated based on the standard curve (Supplementary Fig. 39).

The standard curves of the detection kits were established by using plasmid COVID-19 containing cloned target sequence as the standard. The stock of plasmid DNA was determined by spectrophotometric analysis. The mass of one copy DNA was calculated as:

$$m = n \times 1.096 \times 10^{-21}$$

where n is the plasmid size (bp) and m is the mass (g). A series of serial dilutions were performed to achieve a working stock of plasmid DNA. The standard curves for quantitation were obtained by measuring the serially diluted plasmid DNA (Supplementary Figs. 29 and 39).

Device measurement. Source-drain electrodes were wire bonded using Al wires. Then, 80 μl or 100 μl buffer solution (Supplementary Note 3) or biofluids were added into the PDMS well as electrolyte throughout the measurement, and a Ag/AgCl reference electrode was inserted into the solution as the liquid gate electrode⁷⁴. The electrical characterization was carried out at room temperature by using a semiconductor analyser (Keysight, B1500A). After the I_{ds} stabilized, I_{ds} versus V_{lg} curves were obtained by sweeping V_{lg} in a certain range, and the Dirac point was obtained at V_{lg} where I_{ds} reaches its minimum.

To measure targets by using MoEMS g-FETs, the device was first immersed in 80 μl or 100 μl buffer solution or biofluids, and then a stable V_{ds} bias ($V_{\text{ds}} = 50$ mV) was applied between the drain and source electrodes. After the I_{ds} stabilized, time-resolved I_{ds} measurement was performed. To add the testing solutions, 50% or 100% volume solution was taken out from the PDMS well and then was replaced by pre-mixed samples of the same volume. The solutions with a certain concentration of analytes (thrombin, casein, BSA, Hg²⁺, Fe³⁺, Cd²⁺, Zn²⁺, Ca²⁺, Cu²⁺, ATP, CTP, GTP, ss-DNA-T, ss-DNA-R1, ss-DNA-R2, ss-DNA-R3, ss-DNA-mis-3', ss-DNA-mis-m, ss-DNA-mis-5', SARS-CoV-2 cDNA, human cDNA, SARS-CoV-2 IVT RNA, SARS-CoV IVT RNA, MERS-CoV IVT RNA) or clinical samples (P1–P33, F1–F23, A1–A4, B1, B2, H1–H25) were added, and at the same time I_{ds} versus t curves were recorded. To improve the sensitivity, negative V_{lg} (that is, -0.5 V) was applied to drive MoEMS during the measurements. As a comparison, I_{ds} versus t curves were also measured at $V_{\text{lg}} = 0$ V. To conduct measurement in full serum, the MoEMS g-FET devices were immersed in 100% foetal bovine serum (Zhejiang Tianhang Biotechnology) for 2 h before usage.

To conduct measurements in full artificial saliva, the MoEMS g-FET devices were immersed in 100% artificial saliva (Solarbio) for 1 h before usage. To conduct measurements of the clinical samples, the MoEMS g-FET devices were immersed in VTM (Yocon) for ~1–2 h before usage. To conduct measurements in full serum, thrombin, ATP and ss-DNAs were spiked to 100% foetal bovine serum and diluted to different concentrations by adding full serum. To examine the long-term stability, the MoEMS g-FET devices were immersed in 100% foetal bovine serum for 15 days or in VTM for 3, 10, 15 and 21 days, and then electrical measurements were carried out under the same conditions as described above.

The threshold value to diagnose COVID-19 by MoEMS g-FETs was taken from three times the largest response of the negative samples. The diagnosis time was read from the interception of the threshold value and the real-time $\Delta I_{\text{ds}}/I_{\text{ds0}}$ responses. As an example, most $\Delta I_{\text{ds}}/I_{\text{ds0}}$ values of negative samples were below 0.08%; thus, the threshold value was set to 0.24%. The response time of P4, P7, P18, and P21 was therefore ~60 s, ~22 s, ~90 s and ~20 s according to the time when the $\Delta I_{\text{ds}}/I_{\text{ds0}}$ response reached the threshold value (Extended Data Fig. 7), respectively.

Prototype testing system for detecting SARS-CoV-2 nucleic acids. For on-site and point-of-care detection, a prototype of the COVID-19 testing system was assembled by using MoEMS g-FETs (Supplementary Fig. 41). The testing system was composed of two parts. The first was a MoEMS g-FET-integrated testing module, which served as the consumable material in the test. To avoid cross interference between different samples, one module was used for testing one sample. The second was the main system with size of 11.5 cm × 9 cm × 5.5 cm, which included a controller, digital converters, a timer, a rechargeable lithium battery, a signal processing module, a signal amplifier regulator module and a signal output module that could connect with smartphone or computer by USB, WiFi or Bluetooth. The main system was reused for multiple tests by simply replacing the MoEMS testing module. The operation of this system took three steps (Supplementary Fig. 42). The first step was to connect the testing module with the main system and connect the computer or the smartphone with the testing system by USB, Wifi or Bluetooth. The second step was to open the seal

which covered the PDMS well of the testing module. The third step was to add the testing sample into the PDMS well and to read the results from the computer or the smartphone.

Reporting Summary. Further information on research design is available in the Nature Research Reporting Summary linked to this article.

Data availability

The main data supporting the results in this study are available within the paper and its Supplementary Information. The raw and analysed datasets generated during the study are too large to be shared publicly, yet they are available for research purposes from the corresponding authors on reasonable request.

Received: 20 May 2021; Accepted: 17 November 2021;

Published online: 7 February 2022

References

- Anichini, C. et al. Chemical sensing with 2D materials. *Chem. Soc. Rev.* **47**, 4860–4908 (2018).
- Sabaté del Río, J. et al. An antifouling coating that enables affinity-based electrochemical biosensing in complex biological fluids. *Nat. Nanotechnol.* **14**, 1143–1149 (2019).
- Gooding, J. J. & Gaus, K. Single-molecule sensors: challenges and opportunities for quantitative analysis. *Angew. Chem. Int. Ed.* **55**, 11354–11366 (2016).
- Banerjee, I., Pangule, R. C. & Kane, R. S. Antifouling coatings: recent developments in the design of surfaces that prevent fouling by proteins, bacteria, and marine organisms. *Adv. Mater.* **23**, 690–718 (2011).
- Zhang, X. et al. Ultrasensitive field-effect biosensors enabled by the unique electronic properties of graphene. *Small* **16**, 1902820 (2020).
- Jiang, C. et al. Antifouling strategies for selective in vitro and in vivo sensing. *Chem. Rev.* **120**, 3852–3889 (2020).
- Broughton, J. P. et al. CRISPR–Cas12-based detection of SARS-CoV-2. *Nat. Biotechnol.* **38**, 870–874 (2020).
- Real-time RT-PCR panel for detection 2019-nCoV. *US Centers for Disease Control and Prevention* <https://www.cdc.gov/coronavirus/2019-ncov/lab/rt-pcr-detection-instructions.html> (2020).
- Validation Report of Real-time RT-PCR Panel for Detection of 2019-nCoV (China National Center for Clinical Laboratories, 2020); <https://projectscreen.co/validation-report.pdf>
- Chan, J. F. et al. Improved molecular diagnosis of COVID-19 by the novel, highly sensitive and specific COVID-19-RdRp/Hel real-time reverse transcription-PCR assay validated in vitro and with clinical specimens. *J. Clin. Microbiol.* **58**, e00310–e00320 (2020).
- Chan, J. F. et al. A familial cluster of pneumonia associated with the 2019 novel coronavirus indicating person-to-person transmission: a study of a family cluster. *Lancet* **395**, 514–523 (2020).
- Pan, Y., Zhang, D., Yang, P., Poon, L. L. M. & Wang, Q. Viral load of SARS-CoV-2 in clinical samples. *Lancet Infect. Dis.* **20**, 411–412 (2020).
- Pravin, P., Chang, H. & Han, M. Detecting the coronavirus (COVID-19). *ACS Sens.* **5**, 2283–2296 (2020).
- Service, R. F. Fast, cheap tests could enable safer reopening. *Science* **369**, 608–609 (2020).
- Ekinci, K. L. Electromechanical transducers at the nanoscale: actuation and sensing of motion in nanoelectromechanical systems (NEMS). *Small* **1**, 786–797 (2005).
- Blencowe, M. P. Nanoelectromechanical systems. *Contemp. Phys.* **46**, 249–264 (2005).
- Craighead, H. G. Nanoelectromechanical systems. *Science* **290**, 1532–1535 (2000).
- Barba, P. D. & Wiak, S. *MEMS: Field Models and Optimal Design* (Springer Nature, 2020).
- Ohno, Y., Maehashi, K. & Matsumoto, K. Label-free biosensors based on aptamer-modified graphene field-effect transistors. *J. Am. Chem. Soc.* **132**, 18012–18013 (2010).
- Zhang, A. & Lieber, C. M. Nano-bioelectronics. *Chem. Rev.* **116**, 215–257 (2016).
- Nakatsuka, N. et al. Aptamer–field-effect transistors overcome Debye length limitations for small-molecule sensing. *Science* **362**, 319–324 (2018).
- Hwang, M. T. et al. DNA nanotweezers and graphene transistor enable label-free genotyping. *Adv. Mater.* **30**, 1802440 (2018).
- Gao, N. et al. General strategy for biodetection in high ionic strength solutions using transistor-based nanoelectronic sensors. *Nano Lett.* **15**, 2143–2148 (2015).
- Stern, E. et al. Importance of the Debye screening length on nanowire field effect transistor sensors. *Nano Lett.* **7**, 3405–3409 (2007).
- Wilson, J. & Hunt, T. *Molecular Biology of the Cell: A Problems Approach* 4th edn (Garland Science, 2002).
- Kaisti, M. Detection principles of biological and chemical FET sensors. *Biosens. Bioelectron.* **98**, 437–448 (2017).
- An, T., Kim, K. S., Hahn, S. K. & Lim, G. Real-time, step-wise, electrical detection of protein molecules using dielectrophoretically aligned SWNT-film FET aptasensors. *Lab Chip* **10**, 2052–2056 (2010).
- An, J. H., Park, S. J., Kwon, O. S., Bae, J. & Jang, J. High-performance flexible graphene aptasensor for mercury detection in mussels. *ACS Nano* **7**, 10563–10571 (2013).
- Xu, S. et al. Graphene foam field-effect transistor for ultra-sensitive label-free detection of ATP. *Sens. Actuators B* **284**, 125–133 (2019).
- Hajian, R. et al. Detection of unamplified target genes via CRISPR–Cas9 immobilized on a graphene field-effect transistor. *Nat. Biomed. Eng.* **3**, 427–437 (2019).
- Park, S. J. et al. Ultrasensitive flexible graphene based field-effect transistor (FET)-type bioelectronic nose. *Nano Lett.* **12**, 5082–5090 (2012).
- Kurnik, M., Pang, E. Z. & Plaxco, K. W. An electrochemical biosensor architecture based on protein folding supports direct real-time measurements in whole blood. *Angew. Chem. Int. Ed.* **59**, 18442–18445 (2020).
- Quijano-Rubio, A. et al. De novo design of modular and tunable protein biosensors. *Nature* **591**, 482–487 (2021).
- Lin, M. et al. Electrochemical detection of nucleic acids, proteins, small molecules and cells using a DNA-nanostructure-based universal biosensing platform. *Nat. Protoc.* **11**, 1244–1263 (2016).
- Goodman, R. P. et al. Rapid chiral assembly of rigid DNA building blocks for molecular nanofabrication. *Science* **310**, 1661–1665 (2005).
- Bock, L. C., Griffin, C., Vermaas, E. H. & Toole, J. J. Selection of single-stranded DNA molecules that bind and inhibit human thrombin. *Nature* **355**, 564–566 (1992).
- Ono, A. & Togashi, H. Highly selective oligonucleotide-based sensor for mercury(II) in aqueous solutions. *Angew. Chem. Int. Ed.* **43**, 4300–4302 (2004).
- Mukherjee, S. et al. A graphene and aptamer based liquid gated FET-like electrochemical biosensor to detect adenosine triphosphate. *IEEE Trans. Nanobiosci.* **14**, 967–972 (2015).
- Dunn, M. R., Jimenez, R. M. & Chaput, J. C. Analysis of aptamer discovery and technology. *Nat. Rev. Chem.* **1**, 0076 (2017).
- Kopperger, E. et al. A self-assembled nanoscale robotic arm controlled by electric fields. *Science* **359**, 296–301 (2018).
- Ranganathan, S. V. et al. Complex thermodynamic behavior of single-stranded nucleic acid adsorption to graphene surfaces. *Langmuir* **32**, 6028–6034 (2016).
- Wang, Z. et al. Free radical sensors based on inner-cutting graphene field-effect transistors. *Nat. Commun.* **10**, 1544 (2019).
- Huizenga, D. E. & Szostak, J. W. A DNA aptamer that binds adenosine and ATP. *Biochemistry* **34**, 656–665 (1995).
- Seo, G. et al. Rapid detection of COVID-19 causative virus (SARS-CoV-2) in human nasopharyngeal swab specimens using field-effect transistor based biosensor. *ACS Nano* **14**, 5135–5144 (2020).
- Guo, K. et al. Rapid single-molecule detection of COVID-19 and MERS antigens via nanobody-functionalized organic electrochemical transistors. *Nat. Biomed. Eng.* **5**, 666–677 (2021).
- Chu, D. K. W. et al. Molecular diagnosis of a novel coronavirus (2019-nCoV) causing an outbreak of pneumonia. *Clin. Chem.* **66**, 549–555 (2020).
- Gibani, M. M. et al. Assessing a novel, lab-free, point-of-care test for SARS-CoV-2 (CovidNudge): a diagnostic accuracy study. *Lancet Microbe* **1**, e300–e307 (2020).
- CDC 2019-Novel Coronavirus (2019-nCoV) Real-time RT-PCR Diagnostic Panel (Centers for Disease Control and Prevention, 2020); <https://www.fda.gov/media/134922/download>
- Nelson, A. C. et al. Analytical validation of a COVID-19 qRT-PCR detection assay using a 384-well format and three extraction methods. Preprint at. bioRxiv, <https://doi.org/10.1101/2020.04.02.022186> (2020)..
- Yu, L. et al. Rapid colorimetric detection of COVID-19 coronavirus using a reverse transcriptional loop-mediated isothermal amplification (RT-LAMP) diagnostic platform: iLACO. *Clin. Chem.* **66**, 975–977 (2020).
- Baek, Y. H. et al. Development of a reverse transcription-loop-mediated isothermal amplification as a rapid early-detection method for novel SARS-CoV-2. *Emerg. Microbes Infect.* **9**, 998–1007 (2020).
- Yang, W. et al. Rapid detection of SARS-CoV-2 using reverse transcription RT-LAMP method. Preprint at. medRxiv, <https://doi.org/10.1101/2020.03.02.20030130> (2020)..
- Patchsung, M. et al. Clinical validation of a Cas13-based assay for the detection of SARS-CoV-2 RNA. *Nat. Biomed. Eng.* **4**, 1140–1149 (2020).
- Ding, X. et al. Ultrasensitive and visual detection of SARS-CoV-2 using all-in-one dual CRISPR-Cas12a assay. *Nat. Commun.* **11**, 4711 (2020).
- Behrmann, O. et al. Rapid detection of SARS-CoV-2 by low volume real-time single tube reverse transcription recombinase polymerase amplification using an exo probe with an internally linked quencher (Exo-IQ). *Clin. Chem.* **66**, 1047–1054 (2020).

56. Zhang, F., Abudayyeh, O. O. & Jonathan, S. G. A Protocol for Detection of COVID-19 Using CRISPR Diagnostics (Broad Institute, 2020); [https://www.broadinstitute.org/files/publications/special/COVID-19%20detection%20\(updated\).pdf](https://www.broadinstitute.org/files/publications/special/COVID-19%20detection%20(updated).pdf)
57. Xue, G. et al. A reverse transcription recombinase-aided amplification assay for rapid detection of the 2019 novel coronavirus (SARS-CoV-2). *Anal. Chem.* **92**, 9699–9705 (2020).
58. Qiu, G. et al. Thermoplasmonic-assisted cyclic cleavage amplification for self-validating plasmonic detection of SARS-CoV-2. *ACS Nano* **15**, 7536–7546 (2021).
59. Zhao, H. et al. Ultrasensitive super sandwich-type electrochemical sensor for SARS-CoV-2 from the infected COVID-19 patients using a smartphone. *Sens. Actuators B* **327**, 128899–128908 (2021).
60. Chaibun, T. et al. Rapid electrochemical detection of coronavirus SARS-CoV-2. *Nat. Commun.* **12**, 802 (2020).
61. Alafeef, M., Dighe, K., Moitra, P. & Pan, D. Rapid, ultrasensitive, and quantitative detection of SARS-CoV-2 using antisense oligonucleotides directed electrochemical biosensor chip. *ACS Nano* **14**, 17028–17045 (2020).
62. Nachtigall, F. M., Pereira, A., Trofymchuk, O. S. & Santos, L. S. Detection of SARS-CoV-2 in nasal swabs using MALDI-MS. *Nat. Biotechnol.* **38**, 1168–1173 (2020).
63. Ihling, C. et al. Mass spectrometric identification of SARS-CoV-2 proteins from gargle solution samples of COVID-19 patients. *J. Proteome Res.* **19**, 4389–4392 (2020).
64. Li, X. S. et al. Large-area synthesis of high-quality and uniform graphene films on copper foils. *Science* **324**, 1312–1314 (2009).
65. Gao, L. et al. Repeated growth and bubbling transfer of graphene with millimetre-size single-crystal grains using platinum. *Nat. Commun.* **3**, 699 (2012).
66. Wang, X., Hao, Z., Olsen, T. R., Zhang, W. & Lin, Q. Measurements of aptamer–protein binding kinetics using graphene field-effect transistors. *Nanoscale* **11**, 12573 (2019).
67. Reina, A. et al. Layer area, few-layer graphene films on arbitrary substrates by chemical vapor deposition. *Nano Lett.* **8**, 30–35 (2009).
68. August, B. “Bestimmung der Absorption des rothen Lichts in farbigen Flüssigkeiten” (Determination of the absorption of red light in colored liquids). *Ann. Phys. Chem.* **86**, 78–88 (1852).
69. Lin, M. et al. Programmable engineering of a biosensing interface with tetrahedral DNA nanostructures for ultrasensitive DNA detection. *Angew. Chem. Int. Ed.* **54**, 2151–2155 (2015).
70. Hao, Z. et al. Real-Time monitoring of insulin using a graphene field-effect transistor aptameric nanosensor. *ACS Appl. Mater. Interfaces* **9**, 27504–27511 (2017).
71. Lin, M. et al. Programmable engineering of a biosensing interface with tetrahedral DNA nanostructures for ultrasensitive DNA detection. *Angew. Chem. Int. Ed.* **54**, 2151–2155 (2015).
72. Chen, Z. et al. Energy transfer from individual semiconductor nanocrystals to graphene. *ACS Nano* **4**, 2964–2968 (2010).
73. Rong, Z. et al. Isolation of a 2019 novel coronavirus strain from a coronavirus disease 19 patient in Shanghai. *J. Microbes Infect.* **15**, 111–121 (2020).
74. Hwang, M. T. et al. Highly specific SNP detection using 2D graphene electronics and DNA strand displacement. *Proc. Natl Acad. Sci. USA* **113**, 7088–7093 (2016).

Acknowledgements

We thank K. Vesterager Gothelf from Aarhus University for the valuable discussion on this research. This work was supported by the National Key R&D Program of China (2021YFE0201400), the National Natural Science Foundation of China (51773041, 61890940, 21603038), the Shanghai Committee of Science and Technology in China (18ZR1404900), the Chongqing Bayu Scholar Program (DP2020036), the Strategic Priority Research Program of the Chinese Academy of Sciences (XDB30000000), the China Postdoctoral Science Foundation (2019M661338, 2016LH00046, 2019M661353), the National Postdoctoral Program for Innovative Talents (BX20190072), the Major Project of MOST in China (2018ZX10714002-001-005) and biosafety level 3 laboratory of Fudan University.

Author contributions

D.W. supervised the project. D.W. conceived the original idea and designed all aspects of the experiments. L.W. and Y.G.W. prepared MoEMS. X.W., Y.G.W. and D.K. fabricated devices. L.W. did AFM, transmission electron microscopy, Raman, scanning electron microscopy and gel electrophoresis. X.W., C.Z., C.D. and L.W. did fluorescence measurements. X.W. measured FRET. C.G., Y.W., D.Q. and Y.X. prepared SARS-CoV-2 virus cDNA samples. M.G. and Z.Z. provided clinical samples. C.G., Y.X., M.G. and Z.Z. measured qRT-PCR. X.W., Y.G.W., C.D., D.K. and D.W. measured devices. D.W., L.W., X.W., Y.G.W., Y.L. and C.F. analysed the data and prepared the manuscript. All authors commented on the manuscript.

Competing interests

The authors declare no competing interests.

Additional information

Extended data is available for this paper at <https://doi.org/10.1038/s41551-021-00833-7>.

Supplementary information The online version contains supplementary material available at <https://doi.org/10.1038/s41551-021-00833-7>.

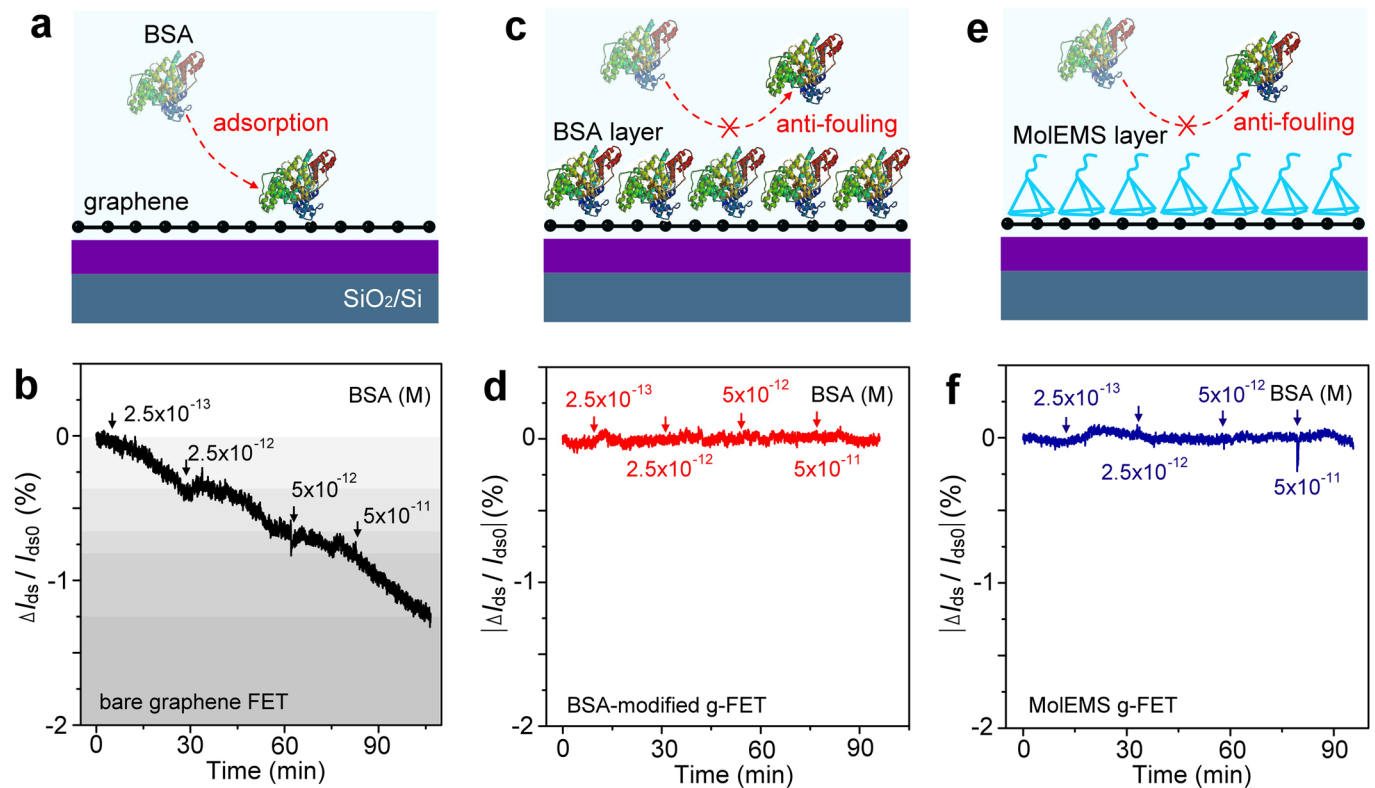
Correspondence and requests for materials should be addressed to Zhaoqin Zhu or Dacheng Wei.

Peer review information *Nature Biomedical Engineering* thanks the anonymous reviewer(s) for their contribution to the peer review of this work.

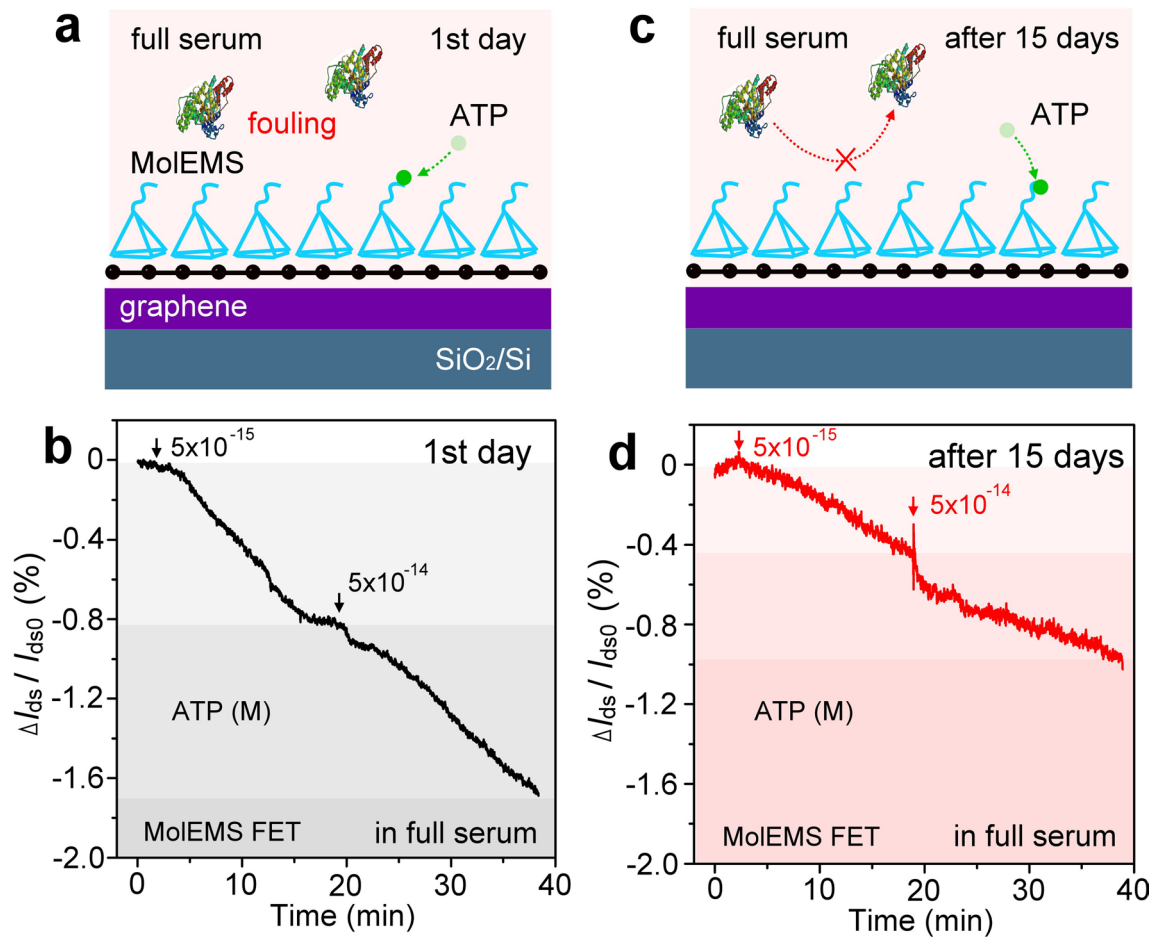
Reprints and permissions information is available at www.nature.com/reprints.

Publisher's note Springer Nature remains neutral with regard to jurisdictional claims in published maps and institutional affiliations.

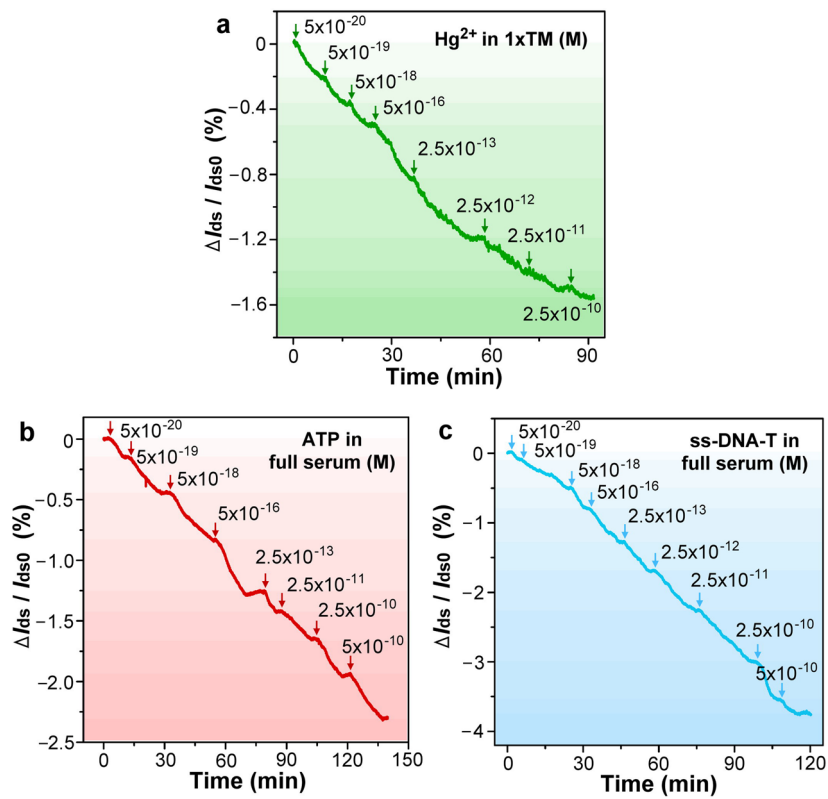
© The Author(s), under exclusive licence to Springer Nature Limited 2022



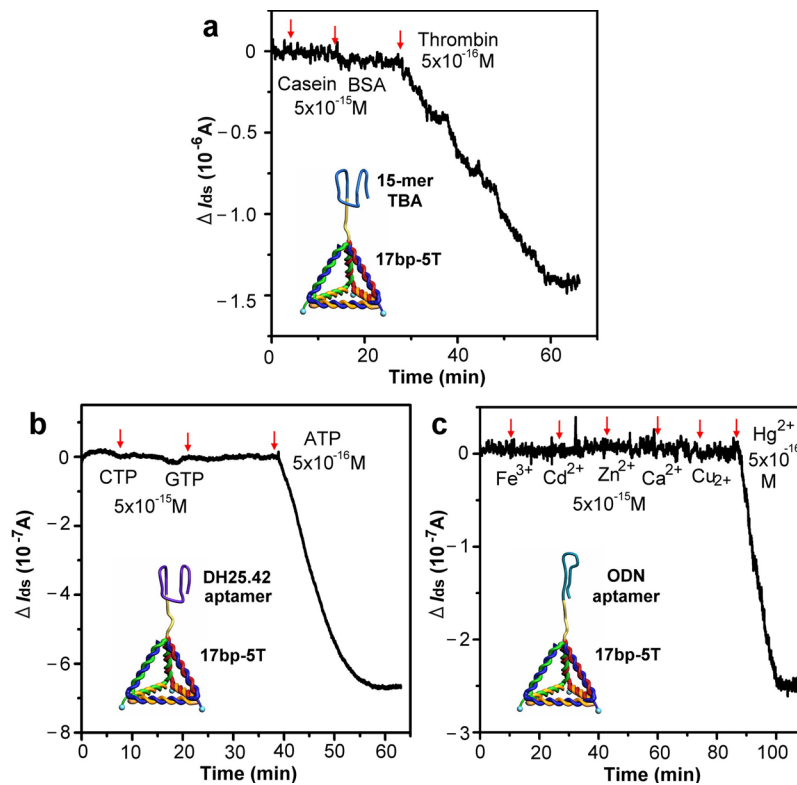
Extended Data Fig. 1 | Antifouling performance against BSA. **a, b**, $\Delta I_{ds}/I_{ds0}$ responses of a bare g-FET upon addition of BSA with concentrations from 2.5×10^{-13} M to 5×10^{-11} M in 1xTM buffer. **c, d**, $\Delta I_{ds}/I_{ds0}$ responses of a g-FET modified with a BSA antifouling layer upon addition of BSA with concentrations from 2.5×10^{-13} M to 5×10^{-11} M in 1xTM buffer. To modify the graphene surface with the BSA layer, we added 50 μ L 1xTM buffer solution with 1×10^{-3} M BSA in the PDMS well of the device. After 12-hours incubation, the g-FET was washed using 1xTM buffer by three times. **e, f**, $\Delta I_{ds}/I_{ds0}$ responses of a MoIEMS g-FET upon addition of BSA with concentrations from 2.5×10^{-13} M to 5×10^{-11} M in 1xTM buffer. The MoIEMS g-FET exhibits an antifouling ability against unspecific adsorption of BSA. All samples were technical replicates.



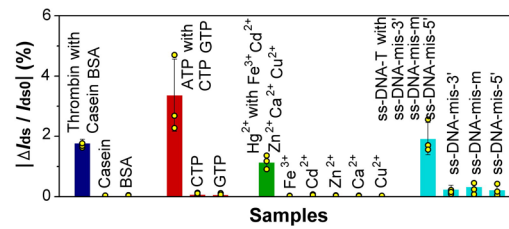
Extended Data Fig. 2 | Long-term stability of the MoIEMS g-FETs. **a, b**, $\Delta I_{ds} / I_{ds0}$ responses of a MoIEMS g-FET with DH25.42 aptamer probes upon addition of 5×10^{-15} M and 5×10^{-14} M ATP in full serum. **c, d**, $\Delta I_{ds} / I_{ds0}$ responses of the same MoIEMS g-FET device upon addition of 5×10^{-15} M and 5×10^{-14} M ATP in full serum, after continuous exposure in full serum for 15 days at 4 °C. The response maintains -56% in full serum after 15 days. All samples were technical replicates.



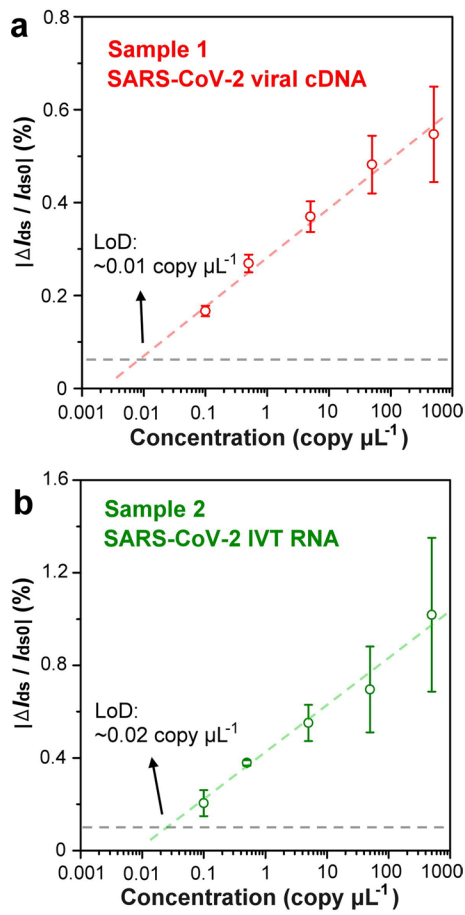
Extended Data Fig. 3 | Real-time detection of Hg^{2+} , ATP and ss-DNA. $\Delta I_{ds} / I_{ds0}$ responses of MoEMS g-FETs with corresponding probes upon addition of (a) Hg^{2+} (1xTM), (b) ATP (full serum) and (c) ss-DNA-T (full serum) with concentrations from 5×10^{-20} M to 2.5×10^{-10} or 5×10^{-10} M under an electrostatic actuation. All samples were technical replicates.



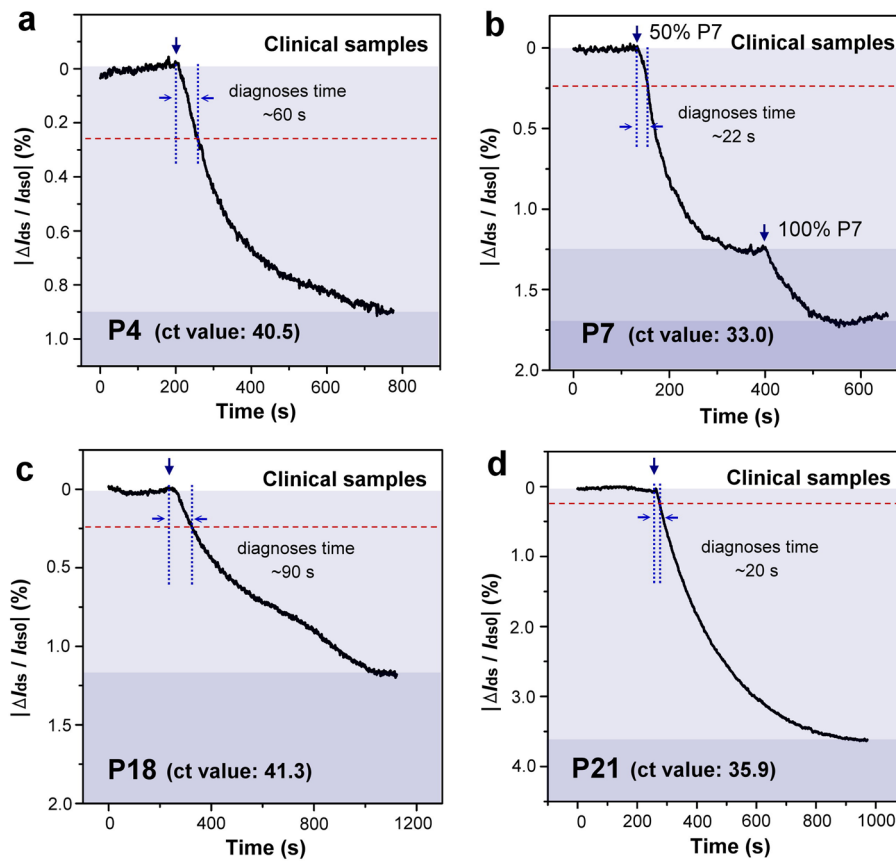
Extended Data Fig. 4 | Selectivity of the MolEMS g-FET sensors. Real-time ΔI_{ds} responses of MolEMS g-FETs carrying different probes upon targeted (5×10^{-16} M) and non-targeted (5×10^{-15} M) analytes. **a**, The targeted analyte is thrombin, and non-targeted analytes are Casein and BSA. **b**, The targeted analyte is ATP, and non-targeted analytes are CTP and GTP. **c**, The targeted analyte is Hg^{2+} , and non-targeted analytes are Fe^{3+} , Cd^{2+} , Zn^{2+} , Ca^{2+} and Cu^{2+} . All samples were technical replicates.



Extended Data Fig. 5 | Specificity towards mixture samples. $|\Delta I_{ds}/I_{ds0}|$ responses of MoEMS g-FETs upon non-targeted (5×10^{-15} M) analytes and upon mixture samples with the targeted analytes (5×10^{-16} M) and non-targeted analytes (5×10^{-15} M). The mixed samples are a mixture of 5×10^{-16} M Thrombin, 5×10^{-15} M Casein, 5×10^{-15} M BSA; a mixture of 5×10^{-16} M ATP, 5×10^{-15} M CTP, 5×10^{-15} M GTP; a mixture of 5×10^{-16} M Hg²⁺, 5×10^{-15} M Fe³⁺, 5×10^{-15} M Cd²⁺, 5×10^{-15} M Zn²⁺, 5×10^{-15} M Ca²⁺, 5×10^{-15} M Cu²⁺; and a mixture of 5×10^{-16} M ss-DNA-T, 5×10^{-15} M ss-DNA-mis-3', 5×10^{-15} M ss-DNA-mis-m, 5×10^{-15} M ss-DNA-mis-5'. All samples were technical replicates.



Extended Data Fig. 6 | Calculation of the LoD. The LoD values were obtained from the interception of the noise level and the linear standard curve of $|\Delta I_{ds} / I_{ds0}|$ versus concentration for the SARS-CoV-2 viral cDNA (**a**) and the SARS-CoV-2 IVT RNA (**b**) detection. The error bars are defined by the standard deviation of the results from 3 parallel experiments. In high concentration region, the larger error bars are probably attributed to the difference of the probe density on each device. All samples were technical replicates.



Extended Data Fig. 7 | Real-time detection of clinical samples from COVID-19 patients. $|\Delta I_{ds} / I_{ds0}|$ versus t curves upon addition of clinical samples (a) P4, (b) 50% and 100% P7, (c) P18 and (d) P21. All samples were biological replicates.

Reporting Summary

Nature Portfolio wishes to improve the reproducibility of the work that we publish. This form provides structure for consistency and transparency in reporting. For further information on Nature Portfolio policies, see our [Editorial Policies](#) and the [Editorial Policy Checklist](#).

Statistics

For all statistical analyses, confirm that the following items are present in the figure legend, table legend, main text, or Methods section.

n/a Confirmed

- | | | |
|-------------------------------------|-------------------------------------|--|
| <input type="checkbox"/> | <input checked="" type="checkbox"/> | The exact sample size (n) for each experimental group/condition, given as a discrete number and unit of measurement |
| <input type="checkbox"/> | <input checked="" type="checkbox"/> | A statement on whether measurements were taken from distinct samples or whether the same sample was measured repeatedly |
| <input checked="" type="checkbox"/> | <input type="checkbox"/> | The statistical test(s) used AND whether they are one- or two-sided
<i>Only common tests should be described solely by name; describe more complex techniques in the Methods section.</i> |
| <input checked="" type="checkbox"/> | <input type="checkbox"/> | A description of all covariates tested |
| <input checked="" type="checkbox"/> | <input type="checkbox"/> | A description of any assumptions or corrections, such as tests of normality and adjustment for multiple comparisons |
| <input type="checkbox"/> | <input checked="" type="checkbox"/> | A full description of the statistical parameters including central tendency (e.g. means) or other basic estimates (e.g. regression coefficient) AND variation (e.g. standard deviation) or associated estimates of uncertainty (e.g. confidence intervals) |
| <input checked="" type="checkbox"/> | <input type="checkbox"/> | For null hypothesis testing, the test statistic (e.g. F , t , r) with confidence intervals, effect sizes, degrees of freedom and P value noted
<i>Give P values as exact values whenever suitable.</i> |
| <input checked="" type="checkbox"/> | <input type="checkbox"/> | For Bayesian analysis, information on the choice of priors and Markov chain Monte Carlo settings |
| <input checked="" type="checkbox"/> | <input type="checkbox"/> | For hierarchical and complex designs, identification of the appropriate level for tests and full reporting of outcomes |
| <input checked="" type="checkbox"/> | <input type="checkbox"/> | Estimates of effect sizes (e.g. Cohen's d , Pearson's r), indicating how they were calculated |

Our web collection on [statistics for biologists](#) contains articles on many of the points above.

Software and code

Policy information about [availability of computer code](#)

Data collection

Data analysis

For manuscripts utilizing custom algorithms or software that are central to the research but not yet described in published literature, software must be made available to editors and reviewers. We strongly encourage code deposition in a community repository (e.g. GitHub). See the Nature Portfolio [guidelines for submitting code & software](#) for further information.

Data

Policy information about [availability of data](#)

All manuscripts must include a [data availability statement](#). This statement should provide the following information, where applicable:

- Accession codes, unique identifiers, or web links for publicly available datasets
- A description of any restrictions on data availability
- For clinical datasets or third party data, please ensure that the statement adheres to our [policy](#)

The main data supporting the results in this study are available within the paper and its Supplementary Information. The raw and analysed datasets generated during the study are too large to be publicly shared, yet they are available for research purposes from the corresponding authors on reasonable request.

Field-specific reporting

Please select the one below that is the best fit for your research. If you are not sure, read the appropriate sections before making your selection.

Life sciences Behavioural & social sciences Ecological, evolutionary & environmental sciences

For a reference copy of the document with all sections, see [nature.com/documents/nr-reporting-summary-flat.pdf](https://www.nature.com/documents/nr-reporting-summary-flat.pdf)

Life sciences study design

All studies must disclose on these points even when the disclosure is negative.

Sample size	For COVID-19 clinical-sample testing (33 positive samples and 54 negative samples), no statistical test was used to determine the sample size. On the basis of the minimal variance observed among technical replicates in pilot experiments, we selected 3 or more technical replicates per sample.
Data exclusions	No data were excluded.
Replication	All the experiments were reproducible.
Randomization	The clinical samples were randomly selected when testing with MoEMS.
Blinding	When measuring clinical samples by MoEMS, the researchers were blinded to the Ct values (qRT-PCR) of the samples.

Reporting for specific materials, systems and methods

We require information from authors about some types of materials, experimental systems and methods used in many studies. Here, indicate whether each material, system or method listed is relevant to your study. If you are not sure if a list item applies to your research, read the appropriate section before selecting a response.

Materials & experimental systems

n/a	Involvement in the study
<input checked="" type="checkbox"/>	<input type="checkbox"/> Antibodies
<input checked="" type="checkbox"/>	<input type="checkbox"/> Eukaryotic cell lines
<input checked="" type="checkbox"/>	<input type="checkbox"/> Palaeontology and archaeology
<input checked="" type="checkbox"/>	<input type="checkbox"/> Animals and other organisms
<input type="checkbox"/>	<input checked="" type="checkbox"/> Human research participants
<input checked="" type="checkbox"/>	<input type="checkbox"/> Clinical data
<input checked="" type="checkbox"/>	<input type="checkbox"/> Dual use research of concern

Methods

n/a	Involvement in the study
<input checked="" type="checkbox"/>	<input type="checkbox"/> ChIP-seq
<input checked="" type="checkbox"/>	<input type="checkbox"/> Flow cytometry
<input checked="" type="checkbox"/>	<input type="checkbox"/> MRI-based neuroimaging

Human research participants

Policy information about [studies involving human research participants](#)

Population characteristics	The COVID-19-positive patients were 14 female and 19 male, 20–78 years old. For the negative controls, 54 donors were included (23 females and 31 males; 24–68 years old).
Recruitment	COVID-19-positive patients and negative participants were recruited from the Shanghai Public Health Clinical Center, and were randomly selected.
Ethics oversight	The research was approved by the Shanghai Public Health Clinical Center Ethics Committee.

Note that full information on the approval of the study protocol must also be provided in the manuscript.